Sound reflection at the open end of axisymmetric ducts issuing a subsonic mean flow: A numerical study

A.R. da Silva [*,1], G.P. Scavone, A. Lefebvre [2]

Computational Acoustic Modeling Laboratory, McGill University, 555 Sherbrooke Street West, Montreal, Canada H3A 1E3

A R T I C L E   I N F O

A B S T R A C T

This paper investigates the reflection of sound waves as they propagate toward the open end of ducts issuing a cold subsonic mean flow in a stagnant fluid. The investigations are conducted by using a relatively new one-step numerical technique known as the lattice Boltzmann method. The results obtained in terms of end correction, l, and magnitude of the pressure reflection coefficient, $|R|$, for an unflanged pipe model are in very good agreement with theoretical predictions and experimental data for the range of Mach numbers $M \leq 0.15$ and Helmholtz numbers $ka \leq 1.5$. Simulations carried out for a similar pipe terminated by circular horns of different curvature radii show that $|R|$ is independent of the horn geometry for Strouhal numbers $Sr_0 < 4$, $Sr_0 = ka/M$. For situations in which $M > 0$, the amplification of the reflection coefficient magnitude, that is $|R| > 1$, is normally ~ 20 percent higher than that observed for an unflanged pipe issuing an equal Mach number flow. Furthermore, the amplification maxima is found to occur always at $Sr_0 = \pi/2$, regardless of whether the pipe is unflanged or terminated by different circular horns. Conversely, the results for the end correction are strongly dependent on the horn curvature. For the low Strouhal number limit, the dimensionless end correction measured at the junction between the horn and the pipe with radius a becomes $l/a = 0.31$ for a horn whose curvature radius is $2a$, and $l/a = 0.62$ for a horn with curvature radius equal to $4a$.

© 2009 Elsevier Ltd. All rights reserved.

1. Introduction

The prediction of the parameters associated with the reflection of sound waves as they approach the open end of ducts issuing a subsonic mean flow is a long-established problem in acoustics. These parameters, particularly the magnitude of the pressure reflection coefficient $|R|$ and the end correction l, are paramount to correctly estimate the proportion of radiated sound and the resonance frequencies of exhaust systems such as those found in aeroengines, tailpipes, nozzles and also woodwind music instruments.

Early theoretical approximations of wave reflection and transmission at the open end of unflanged pipes carrying a cold subsonic mean flow were derived by Carrier [1], who formulated the problem by assuming a uniform (plug) flow, and by Mani [2] and Savkar [3] who provided approximate theories based on flow mismatch between the issuing jet and the ambient fluid. A first exact expression for the far-field radiation was proposed by Munt [4] based on the Wiener–Hopf technique, and was a continuation of the previous solution derived by Levine and Schwinger [5] for an unflanged pipe carrying a zero mean flow. This solution served as a basis for the development of approximate solutions for the dimensionless end correction l/a and magnitude

* Corresponding author. Tel.: +1 514 3984400x094836.
  E-mail address: andrey.dasilva@mcgill.ca (A.R. da Silva).
  [1] Supported by CAPES, Brazil.
  [2] Supported by FQRNT, Canada.

of the reflection coefficient $|R|$ at the open end by Cargill [6,7] and Rienstra [8]. The solutions proposed by Cargill [6] predict that $|R| \to 1$ as $ka \to 0$ and are based on two different approaches that use a Kutta and a non-Kutta condition at the rim of the open end. Later, Cargill [7] predicted that $|R|$ may assume values higher than unity at the critical region $Sr_0 \approx \pi$, where $Sr_0 = 2\pi fa/\bar{u}_o$ is the Strouhal number, f is the frequency of the acoustic field inside the pipe, a is the open-end radius and $\bar{u}_o$ is the cross-sectional averaged mean flow velocity. This prediction agreed with previous experimental investigations conducted by Mechel et al. [9] and by Ronneberger [10]. The low-frequency solution proposed by Rienstra [8] predicted that $l/a \to 0.2554\sqrt{1 - M^2}$ as $ka \to 0$. This prediction has been also confirmed by subsequent experiments conducted by Davies [11] and by Peters et al. [12].

The first exact solution for the magnitude of the reflection coefficient at the open end of thin-walled pipes issuing a subsonic mean flow was presented by Munt [13]. The major characteristic of this solution is the assumption of a uniform flow and a full Kutta condition at the edges of the open end to provide values for the range of $0 \leq ka \leq 1.5$ and $M < 0.3$. This solution has been experimentally validated by Peters et al. [12] using the two-microphone method for $ka < 0.3$ and $M < 0.2$. More recently, Allam and Åbom [14] provided an experimental validation for the entire range of Munt's solution using the full wave decomposition method.

Unfortunately, the intricate physics involved in the problem restricts the application of the analytical approach to very simple geometries such as the unflanged circular duct, although approximate solutions for more complex annular unflanged ducts have been proposed in [15,16]. In practice, the geometric characteristics of real outlet systems, such as nozzles, diffusers, tailpipes, air horns and wind instruments, differ significantly from these simple tubes. In this case, a numerical approach is more suitable.

Numerical approaches have been extensively used to predict acoustic wave reflection and radiation from outlet systems carrying a mean flow. The traditional computational aeroacoustic (CAA) techniques used to tackle this family of problems are, in most cases, based on the *continuum theory*. That is to say, the temporal evolution of both the flow and the acoustic fields is rendered by solving linearized and truncated forms of the partial differential equations that govern the problem, generally the unsteady compressed form of the Navier–Stokes equations. As examples, Chen et al. [17] predicted the far-field normal-mode radiation from an unflanged cylinder using the linearized and integral solutions of Euler and Ffowcs Williams/Hawkings equations. The same problem was approached by Özyörük and Long [18] using a three-dimensional Euler solver coupled with the Kirchhoff method and by Rumsey et al. [19] using a Navier–Stokes indirect solver coupled with the Kirchhoff method.

The use of computational aeroacoustics to predict the variables associated with wave reflection at the open end represents an extremely demanding approach from the computational point of view. This is because the flow–acoustic interaction involved in the problem requires the simultaneous solutions of the entire range of spatial and temporal scales associated with the acoustic and the fluid fields. In this case, an extremely refined space-temporal discretization of the model is paramount to minimize the intrinsic numerical dissipation and dispersion of sound waves. Moreover, the correct representation of the absorbing boundary condition at the surroundings of the model normally involves complex numerical schemes, which substantially increases computational demand.

This paper has two goals. The first is to provide a simple second-order accurate numerical approach to represent reflection phenomena at the open end of axisymmetric ducts carrying a viscous subsonic mean flow. The second goal is focused on conducting a numerical investigation of the acoustic wave reflection in pipes terminated by circular horns with different curvature radii. The two goals are achieved by developing an axisymmetric model of a semi-infinite cylinder based on a *nonequilibrium* technique known as the lattice Boltzmann method (LBM).

For the specific problems addressed in this paper, the lattice Boltzmann method provides several advantages when compared to traditional computational aeroacoustic techniques. These include its relatively straightforward boundary condition schemes and the capability of resolving fully viscous flow problems. As a consequence, the imposition of a Kutta condition to capture vorticity shedding and vorticity generation at the vicinity of a solid boundary and/or boundary layers becomes unnecessary. Furthermore, the lattice Boltzmann method resolves, in a single time-step, both scales associated with the acoustic and flow fields. It is particularly suitable for problems involving high Knudsen numbers ($Kn > 0.1$), which is normally found in shockwaves, high frequency sound and rarefied gases.

The layout of this paper is as follows. The exact analytical solution provided by Munt [13] for unflanged pipes, used here as a benchmark for our numerical approach, is briefly described in Section 2. Section 3 provides an overview of the lattice Boltzmann method and describes the characteristics of the model used in our simulations. The numerical procedures used to obtain the values of the end correction and the magnitude of the reflection function from the model are detailed in Section 4. Section 5 presents the validation of the numerical scheme carried out for an unflanged pipe model. The first part (Section 5.1) compares the fluid dynamic characteristics of the mean flow obtained from the model with the theoretical and experimental data for an axisymmetric free jet, provided in [20–22]. The second part (Section 5.2) compares the results obtained for the sound reflection coefficient R at the open end with theoretical [13] and experimental data [14]. Investigations of the wave reflection at the end of a pipe terminated by circular horns of two different sizes is presented in Section 6. Finally, Section 7 discusses the obtained results.

2. Analytical model

The model derived by Munt [13] predicts the acoustic wave reflections at the open end of circular pipes with rigid thin walls issuing a uniform mean flow with velocity u_x, where the subindex x specifies the axial direction of the pipe. Moreover,
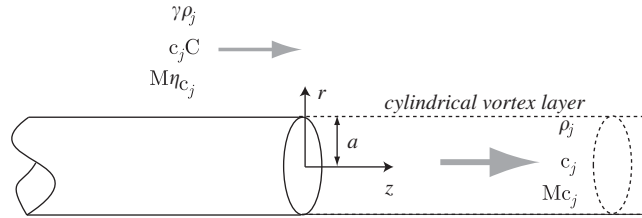
Fig. 1. Representation of the model proposed by Munt [13].

the model takes into account the presence of an external mainstream flow with velocity u_{out} in the same direction of u_x, where the ratio between the outer and the inner flow velocities η is restricted to $0 \leq \eta \leq 1$. It is assumed that the outgoing mean flow forms a jet at the pipe's outlet, which is separated from the ambient fluid by an infinitely thin vortex sheet, as depicted in Fig. 1. The properties of the fluid inside the jet are described in terms of the density ρ_j, the speed of sound c_j and the fluid velocity $Mc_j = u_x$. Likewise, the properties of the ambient fluid outside the thin shear layer are described by the fluid density $\gamma\rho_j$, the speed of sound c_j/C and the fluid speed $M\eta c_j$, where the non-dimensional parameters γ and C are the ratios between the outer and inner jet parameters for fluid density and speed of sound, respectively.

The solution derived by Munt is expressed in terms of integral equations that have been numerically resolved by Bierkens [23], who only considered the calculations of the magnitude of the plane wave reflection coefficient. Later, Panhuis [24] also provided plane wave and higher mode calculations for the phase of the reflection coefficient, and the end correction. These numerical calculations of Munt's solution have been recently verified experimentally by Allam and Åbom [14] using the full wave decomposition method and is correct provided that $M \leq 0.2$ and $0 < ka \leq 1.5$ and that $u'_x/u_x \ll 1$, where u' is the amplitude of the acoustic particle velocity.

3. The lattice Boltzmann method

This section provides a brief overview of the lattice Boltzmann method used in this work. The reader may find a more extended description of the method in a number of books and pioneering articles [25–27]. The lattice Boltzmann method is classified as a *particle* or *nonequilibrium* approach that differs considerably from the traditional techniques based on the *continuum* theory, such as finite differences, finite volumes and boundary elements, to name but a few. While *continuum*-based techniques resolve the governing equations of a system, the lattice Boltzmann method renders the system's temporal macroscopic behavior by simulating two essential operations, namely propagation and collision of fluid particles. In order to perform these operations, the fluid domain is represented in a one-, two- or three-dimensional lattice, depending on the model. The nodes in the lattice are called cells. Each cell comprises N sites, where N is the number of discrete propagation directions of the model.

Fig. 2 depicts the scheme of the lattice model used in this paper, known as D2Q9, after [28]. The cells in the lattice connect to each other by the unity velocity vectors $\mathbf{c}_i$, where the index i indicates the direction of propagation associated with each site. As in the case of the D2Q9 scheme, some models incorporate a null vector $\mathbf{c}_0$ associated with a non-propagating site, which acts to improve the accuracy of the model by removing the unphysical velocity dependency of pressure [29].

In the lattice Boltzmann method, the particles of a fluid are represented in terms of velocity distribution functions. In other words, each particle in the site i of a cell located at $\mathbf{x}$ represents the probability of finding molecules at that specific site, propagating with lattice velocity c and in the direction i. The fundamental operations, namely the propagation and the collision of the fluid particles over the lattice, are then governed by a space-temporal discretization of the Boltzmann equation, known as the lattice Boltzmann equation (LBE), given by

$$F_i(\mathbf{x} + \mathbf{c}_i, t + 1) - F_i(\mathbf{x}, t) = -\frac{1}{\tau}[F_i(\mathbf{x}, t) - F_i^M(\mathbf{x}, t)], \tag{1}$$

where F_i is the distribution function associated with the propagation direction i at the spatial coordinate $\mathbf{x}$ and time t. τ is the relaxation time, which defines the number of particle collisions per unity of time and acts to control the kinematic viscosity of the fluid. F_i^M is the discrete form of the Maxwell distribution function, known as the equilibrium distribution function, which is derived from its continuous counterpart by applying the maximum entropy principle under the constraints of mass and momentum conservation, as described in [26, p. 171]. Thus F_i^M is expressed as

$$F_i^M = \begin{cases} \rho w_i[1 + 3\mathbf{c}_i \cdot \mathbf{u} + \frac{9}{2}(\mathbf{c}_i \cdot \mathbf{u})^2 - \frac{3}{2}\mathbf{u}^2] & \text{for } i = 1, 2, \ldots, 8, \\ \rho[\frac{4}{9} - \frac{2}{3}\mathbf{u}^2] & \text{for } i = 0, \end{cases} \tag{2}$$

where $w_0 = \frac{4}{9}$, $w_{1-4} = \frac{1}{9}$ and $w_{5-8} = \frac{1}{36}$. The axial and radial components of the velocity vectors $\mathbf{c}_i$ are given by

$$\mathbf{c}_0 = (0, 0), \quad \mathbf{c}_{1,3}, \mathbf{c}_{2,4} = (\pm c, 0), (0, \pm c) \quad \text{and} \quad \mathbf{c}_{5,6,7,8} = (\pm c, \pm c), \tag{3}$$
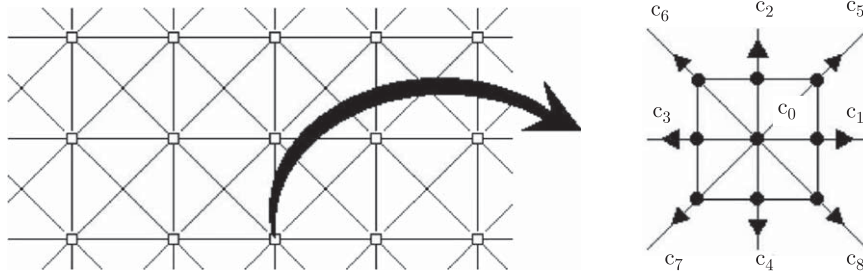
Fig. 2. Representation of a two-dimensional lattice using the squared D2Q9 model.

where the dimensionless speed of sound c in the D2Q9 model is $1/\sqrt{3}$. The local macroscopic variables ρ and $\mathbf{u}$ are obtained in terms of the moments of the local distribution function F_i by

$$\rho(\mathbf{x}, t) = \sum_i F_i(\mathbf{x}, t) \quad \text{and} \quad \rho(\mathbf{x}, t)\mathbf{u}(\mathbf{x}, t) = \sum_i F_i(\mathbf{x}, t)\mathbf{c}_i. \tag{4}$$

The left-hand side of Eq. (1) represents the propagation operator and determines the diffusion of the distribution functions over the lattice. The right-hand term is a simplification of the collision function, which determines the rate at which F_i changes due to intermolecular collisions. This simplification, known as lattice Boltzmann BGK model after Bhatnagar et al. [30], is based on the use of a single relaxation time τ for all directions i.

The isothermal nature of Eq. (1) allows the pressure p and the kinematic viscosity v of the fluid to be given by

$$p = \rho c^2 = \frac{\rho}{3} \quad \text{and} \quad v = \frac{2\tau - 1}{6}. \tag{5}$$

For convenience, the parameters associated with a lattice Boltzmann model are normally described in terms of dimensionless parameters, such as fluid velocity $\mathbf{u}$, space $\mathbf{x}$, time t and viscosity v. However, the physical quantities can be easily obtained from the dimensionless parameters by using the characteristic velocity $\zeta = c^*/c$, and the lattice discretization (pitch) Δx, where c^* is the physical speed of sound. Hence, the physical quantities for velocity $\mathbf{u}^*$, space $\mathbf{x}^*$, time t^*, and viscosity v^* are obtained from their dimensionless counterparts by applying the following relations:

$$\mathbf{u}^* = \zeta\mathbf{u}, \quad \mathbf{x}^* = \Delta x\mathbf{x}, \quad t^* = (\Delta x/\zeta)t \quad \text{and} \quad v^* = \zeta\Delta xv. \tag{6}$$

A very important aspect of the lattice Boltzmann BGK model, as presented above, is the possibility to formally link the microscopic description of the fluid provided by the lattice Boltzmann equation (Eq. (1)) with its macroscopic counterpart, provided by the Navier–Stokes equations. In fact, for slightly compressible flows ($M < 0.15$), the unsteady compressible form of the Navier–Stokes equations can be fully recovered from the isothermal form of the Boltzmann equation (Eq. (1)). This is achieved by performing the Chapman–Enskog expansion, as demonstrated in [28,26].

In recent years, more sophisticated lattice Boltzmann models have been proposed that can recover the unsteady compressible form of the Navier–Stokes equations for higher Mach numbers, namely up to 0.4 [31–33]. This is achieved by taking into account effects of thermal diffusivity and conductivity of the fluid, which become more relevant as flow compressibility grows. In addition, these models normally use multiple relaxation times τ associated with each propagation direction i to increase the model's numerical stability. As a consequence, they become extremely expensive from the computational point of view when compared to the lattice Boltzmann BGK scheme. Thus, considering that the problems addressed in this paper involve Mach numbers ≤ 0.15, the choice of the lattice Boltzmann BGK model is adequate and significantly more economic from the computational viewpoint.

3.1. Axisymmetric lattice Boltzmann model

An important assumption in the simulations carried out in this paper is that the acoustic and fluid dynamic phenomena investigated are symmetric about the duct's axis and thus can be represented by the weakly compressible form of the Navier–Stokes equations in cylindrical polar coordinates, also provided that $M < 0.15$. Following this assumption, the derivatives associated with the azimuthal coordinate, as well as the azimuthal component of velocity vanish, which allows the flow to be simply represented by the axial and radial coordinates, x and r, respectively. Hence the Navier–Stokes equations are expressed in terms of continuity and momentum equations by

$$\frac{\partial \rho}{\partial t} + \frac{\partial(\rho u_x)}{\partial x} + \frac{1}{r}\frac{\partial(\rho r u_r)}{\partial r} = 0, \tag{7}$$

$$\frac{\partial u_x}{\partial t} + u_r\frac{\partial u_x}{\partial r} + u_x\frac{\partial u_x}{\partial x} = -\frac{1}{\rho_0}\frac{\partial p}{\partial x} + v\left[\frac{\partial^2 u_x}{\partial r^2} + \frac{1}{r}\frac{\partial u_x}{\partial r} + \frac{\partial^2 u_x}{\partial x^2}\right], \tag{8}$$

$$\frac{\partial u_r}{\partial t} + u_r \frac{\partial u_r}{\partial r} + u_x \frac{\partial u_r}{\partial x} = -\frac{1}{\rho_0}\frac{\partial p}{\partial r} + v\left[\frac{\partial^2 u_r}{\partial r^2} + \frac{1}{r}\frac{\partial u_r}{\partial r} - \frac{u_r}{r^2} + \frac{\partial^2 u_r}{\partial x^2}\right], \tag{9}$$

where u_x and u_r are the axial and radial components of the velocity, respectively.

Based on the aforementioned assumptions, the simulations carried out in this paper use an adaptation of the lattice Boltzmann equation (Eq. (1)), which was first presented by Halliday [34] and simplified by Reis and Phillips [35]. The adaptation consists in adding a time- and space-dependent source term H_i to the right side of Eq. (1), so that it can fully recover Eqs. (7)–(9) via a Chapman–Enskog expansion. The source term is expressed as

$$H_i = h_i' + h_i'', \tag{10}$$

where h_i' and h_i'' are, respectively, first- and second-order terms as derived by Reis and Phillips [35] and given by

$$h_i' = -\frac{w_i \rho_0 u_r}{r} \tag{11}$$

and

$$h_i'' = \frac{3\varepsilon_i}{y}\left[\frac{c_{iy}^2}{2}\left(u_x\partial_x u_y - \frac{3u_y w_i}{2}Q_{xx} - 3u_y w_i Q_{yy} - \frac{\rho u_y^2}{y}\right) - c_{ix}\left(\frac{6v}{6v+1}Q_{xy} + \frac{\rho}{6}\partial_x u_x - \rho u_x u_y\right)\right.$$
$$\left. + c_{iy}(1-12v)\left(\frac{1}{2(1+6v)}Q_{yy} + \frac{\rho u_y}{y} - \rho u_y^2\right)\right]. \tag{12}$$

The stress $\partial_x u_y$ in Eq. (12) can be approximated by using a spatial finite difference scheme, whereas the tensor Q is given by

$$Q_{\alpha\beta} = \sum_{i=0}^{8} F_i^M c_{i\alpha} c_{i\beta}. \tag{13}$$

The entire derivation of the source terms, as well as the recovery of Eqs. (7)–(9) from Eq. (1) using a Chapman–Enskog expansion is presented in [34,35].

4. Numerical procedures

4.1. The axisymmetric model

The axisymmetric model based on the lattice Boltzmann method is built within a two-dimensional lattice as depicted in Fig. 3. Here and in the following, the parameters associated with the model are expressed in terms of dimensionless lattice quantities.

When representing acoustic wave propagation with the lattice Boltzmann method, the necessary number of lattice nodes (cells) per unity of length of the model depends on the maximum frequency analyzed in the problem. A criterion defined by Wilde [36] establishes that, at least, 12 cells per wavelength (CPW) are necessary in order to reduce the phase speed error to less than 1 percent. However, in the specific case of wave reflection at the open end of ducts, previous investigations by da Silva and Scavone [37] showed that such an error reduction can only be achieved when, at least, 50 CPW are used. In order to meet the criterion observed in [37], the lattice grid depicted in Fig. 3 is built with 500 cells in the
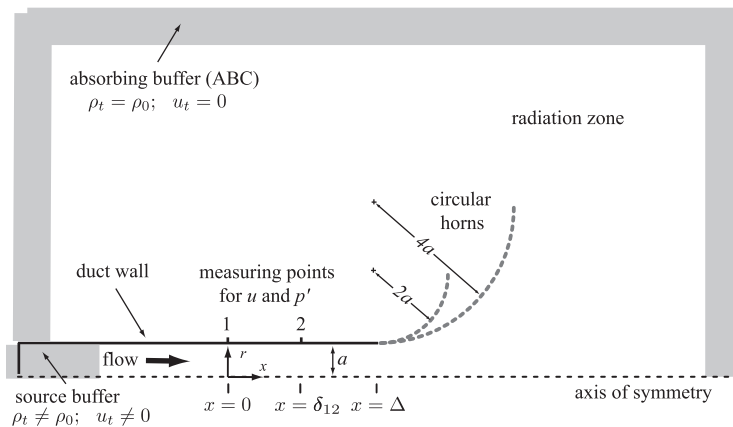
Fig. 3. Scheme of the axisymmetric lattice Boltzmann model for the prediction of the parameters associated with the pressure reflection coefficient at the open end of pipes with different terminations issuing a subsonic mean flow.

horizontal axis and 250 cells in the vertical axis. The pipe is 250 cells long with a radius $a = 20$ cells, and the lattice pitch Δx is equal to 0.001 m. These parameters lead to a minimum discretization of 83 CPW at the maximum frequency of analysis, corresponding to $ka = 1.5$. The thickness of the wall is equal to one cell, which gives a ratio $a/a_o \sim 0.95$, where a_o is the outer radius of the pipe. In this case, the effect of the wall thickness on the reflection coefficient can be neglected when a_0 is used as the reference radius [38].

The grid refinement of a lattice Boltzmann BGK scheme also defines the minimum kinematic viscosity that can be ascribed to the model before it becomes affected by numerical instabilities, as detailed in [27]. For the grid refinement used in this paper, it is found that the minimum dimensionless kinematic viscosity supported by the model corresponds to $v = 7.85 \times 10^{-3}$.

A no-slip boundary condition is applied at the duct wall by using the bounce-back scheme proposed by Bouzidi et al. [39], which acts to invert the propagation direction of the distribution functions F_i just before they reach a solid boundary. This procedure creates a null fluid velocity at the walls and provides results of second-order accuracy to represent viscous boundary layer phenomena. Conversely, a free-slip condition is applied at the lower boundary of the radiation domain that represents the axis of symmetry of the system. Likewise in the previous case, the distribution functions F_i propagating perpendicularly towards a solid boundary are inverted just before the collision, whereas F_i propagating diagonally towards the boundary are reflected in a specular manner.

The top, left and right boundaries of the system are treated with an absorbing boundary condition scheme (ABC) proposed by Kam et al. [40]. This scheme can be seen as an adaptation of the *perfectly matched layer* technique commonly used in computational aeroacoustics schemes [41] and involves creating an asymptotic transition between the fluid density ρ and fluid particle velocity **u** found at the radiation domain and the target parameters ρ_t and $\mathbf{u}_t$, which are imposed at the lattice boundaries. The transition is implemented by using a buffer zone (ABC buffer), as shown in Fig. 3. The non-reflecting condition is achieved by setting $\rho_t = \rho_0$ and $\mathbf{u}_t = 0$, where ρ_0 is the undisturbed density of the fluid. The thickness of the ABC buffer used in the model corresponds to 15 cells and provides a frequency-averaged pressure reflection coefficient of order of magnitude equal to 10^{-3} for both perpendicular and oblique sound incidence. This order of magnitude is smaller than the order of accuracy of the lattice Boltzmann scheme itself, which is 10^{-2}. Hence, the choice of the buffer thickness was considered satisfactory.

The pipe is excited at its input (closed) end with a sinusoidal acoustic source superimposed on a mean flow. The imposition of both the flow and the acoustic sources is attained by using a "source" buffer zone at the input of the pipe. The source buffer is very similar to the ABC buffer used around the radiation zone as a non-reflecting condition. In this case, however, the target parameters u_t and ρ_t assume non-zero values, which forces the buffer to act as a flow–acoustic source instead of an absorbing region. The time-dependent expressions for the target parameters u_t and ρ_t used in the pipe input are given by

$$u_t = \bar{u}_x + H(n - N_t)\bar{u}'_x \sin\left(\frac{3}{2}\frac{n - N_t}{N - N_t}\frac{n\Delta_t c}{a}\right) \tag{14}$$

and

$$\rho_t = \rho_0 + H(n - N_t)\frac{\bar{u}'_x \rho_0}{c}\sin\left(\frac{3}{2}\frac{n - N_t}{N - N_t}\frac{n\Delta_t c}{a}\right), \tag{15}$$

where n and N are, respectively, the nth time step and the total number of time steps in the simulation. $\bar{u}_x$ and $\bar{u}'_x$ are the flow velocity and the acoustic particle velocity amplitude in the axial direction x (Fig. 3). The overbars indicate that the values are averaged along the pipe's cross section. Δ_t is the time increment of the numerical scheme, H is the Heaviside step function given by

$$H = \begin{cases} 0 & \text{for } n < 0, \\ 1 & \text{for } n \geq 0 \end{cases} \tag{16}$$

and N_t is the number of necessary time steps to accelerate the stagnant flow inside the pipe at $n = 0$ to a stationary mean flow with averaged cross section velocity $\bar{u}_x$. Considering that N_t is inversely proportional to the thickness of the source buffer, a buffer of thickness equivalent to 60 cells was used in order to reduce the overall computational time by providing a rapid transient towards the steady state ($N_t \sim 4000$). The choice of a thicker buffer would naturally produce a faster transient but, on the other hand, would not leave enough distance between the end of the source buffer and the first measuring point (point 1) for the flow to become fully developed (see Fig. 3).

The Heaviside function is used in Eqs. (14) and (15) to allow the flow to accelerate from stagnation to a stationary state before the acoustic source, defined by the second terms on the right-hand side of Eqs. (14) and (15), is superimposed. The frequency of the acoustic source varies linearly with time (linear chirp) and sweeps from 0 Hz at $n = N_t$ to a frequency equivalent to $ka = 1.5$ at $n = N$. This corresponds to the range of Helmholtz numbers ka predicted by Munt's theory [13]. Moreover, the ratio $\bar{u}'_x / \bar{u}_x \sim 0.1$ is kept in accordance with the limit of low acoustic amplitude provided in [13].

4.2. Data post-processing

The complex reflection coefficient at the open end of a pipe is given by

$$R = \left(\frac{p_1^+}{p_1^-}\right)\exp(ik\varDelta),\tag{17}$$

where p_1^- and p_1^+ are the reflected and incident wave amplitudes measured inside the pipe at the measuring point 1 (see Fig. 3) and k is the wavenumber.

For plane waves propagating in a viscous mean flow the wavenumber is complex and described by two components $k = k^+ + k^-$, where k^+ and k^- are the components associated with the incident and reflected waves, respectively. The unknowns p^+, p^- and k to be used in Eq. (17) are obtained from a system of equations describing the acoustic field inside the pipe at two different points. The system is constructed by using time histories of the acoustic pressure $p'(t)$ and the cross section averaged value of the acoustic particle velocity $\bar{u}'_x(t)$ measured at points 1 and 2 (see Fig. 3). The equations describing the sound field at point 1 are given by

$$p'_1(f) = p_1^+ + p_1^-\tag{18}$$

and

$$\bar{u}'_{x1}(f) = \frac{1}{\rho_0 c_0}(p_1^+ - p_1^-),\tag{19}$$

where $p'_1(f)$ and $\bar{u}'_{x1}(f)$ are the discrete Fourier transform of the acoustic pressure and acoustic particle velocity time histories $p'_1(t)$ and $\bar{u}'_{x1}(t)$, respectively. Here and in the following, the numerical subindices designate the location of the measuring point as depicted in Fig. 3.

Similarly, the sound field at point 2 is given by

$$p'_2(f) = p_1^+ \exp(-ik^+\delta_{12}) + p_1^- \exp(ik^-\delta_{12})\tag{20}$$

and

$$\bar{u}'_{x2}(f) = \frac{1}{\rho_0 c_0}(p_1^+ \exp(-ik^+\delta_{12}) + p_1^- \exp(ik^-\delta_{12})),\tag{21}$$

where δ_{12} is the distance between the points 1 and 2. Following an analogous procedure discussed in [14], Eqs. (18)–(21) can be rearranged in a system whose solution for the unknowns is given by

$$\begin{Bmatrix} p_1^+ \\ p_1^- \\ A \\ B \end{Bmatrix} = \begin{bmatrix} 1 & 1 & 0 & 0 \\ 0 & 0 & 1 & 1 \\ 1/\rho_0 c_0 & -1/\rho_0 c_0 & 0 & 0 \\ 0 & 0 & 1/\rho_0 c_0 & -1/\rho_0 c_0 \end{bmatrix}^{-1} \begin{Bmatrix} p'_1 \\ p'_2 \\ \bar{u}'_{x1} \\ \bar{u}'_{x2} \end{Bmatrix},\tag{22}$$

where $A = p_1^+ \exp(-ik^+\delta_{12})$ and $B = p_1^+ \exp(ik^-\delta_{12})$. Thus, the incident and reflected wavenumber components are obtained by

$$k^+ = -\frac{1}{i\delta_{12}}\ln\left(\frac{A}{p_1^+}\right) \quad \text{and} \quad k^- = \frac{1}{i\delta_{12}}\ln\left(\frac{B}{p_1^+}\right).\tag{23}$$

Finally, the inertial effect due to the fluid loading at the open end, known as the end correction, is given by

$$l = \text{Re}\left(\frac{1}{i(k^+ + k^-)}\ln\left(\frac{R}{|R|}\right)\right).\tag{24}$$

5. Validation of the numerical scheme

5.1. Fluid field

The characteristics of the mean flow presented below are initially obtained in the absence of the acoustic source at pipe's closed end, as described in Section 4.1. The dynamic characteristics of the flow, such as the velocity profiles downstream and upstream from the pipe's open and, as well as the centerline velocity decay are obtained for the maximum Mach number considered in this paper ($M = 0.15$). This implies a Reynolds number $Re = 2aMc/v = 441$, according to the dimensionless values of kinematic viscosity v, pipe radius a, and lattice speed of sound c ascribed to the model (Section 4.1).

In the absence of the acoustic source at the closed end, when the simulation achieves its steady state ($n{\sim}4000$) the flow is laminar in both upstream and downstream regions from the outlet. Moreover, due to the no-slip boundary condition ascribed to the pipe walls, the upstream flow becomes fully developed at $x = 0$ until the pipe's open end at $x = \varDelta$

(see Fig. 3). Hence, the axial velocity at $0 \leq x \leq \Delta$ can be described by a Hagen–Poiseuille parabolic profile [20], given by

$$u_x = \frac{3}{2}\bar{u}_x\left[1 - \left(\frac{r}{a}\right)^2\right].\tag{25}$$

A dimensionless form of Eq. (25) is achieved by considering the maximum flow velocity at the open end, $u_0 = u_x|_{r=0} = 3\bar{u}_x/2$, which gives

$$\frac{u_x}{u_0} = \left[1 - \left(\frac{r}{a}\right)^2\right].\tag{26}$$

Fig. 4 provides a comparison between numerical and theoretical predictions for the normalized axial velocity profiles at two different points inside the pipe ($x = 0$ and Δ). The velocity profiles obtained numerically indicate that the flow at $0 \leq x \leq \Delta$ is laminar and the agreement with the theory is very good.

As expected, the simulation results show that the discharge of the fully developed upstream flow into the radiation zone forms a free laminar jet downstream from the open end. In this case, the jet can be divided in three distinctive regions along the axial direction x [20,22]. The first region, known as the core zone, extends from the open end to the apex of the jet's potential core. In this region, the centerline velocity remains essentially constant and equal to the open end velocity at the center of the jet u_0. The second region is defined by a small transition between the first and the third regions. In the third region, which is known as the developed zone, the transverse velocity profiles at different distances from the open end are similar and the centerline velocity u_{cl} decays at $1/x$ rate. Measurements of the centerline velocity decay have been conducted by Symons and Labus [20] for round laminar free jets, whose velocity profile at the outlet is fully developed and expressed by Eq. (26). Fig. 5 compares the numerical results for the centerline velocity decay at $Re = 441$ with the experimental results provided by Symons and Labus at $Re = 437$.

The numerical results shown in Fig. 5 agree very well with the experimental data for a region that extends eight pipe radii from the open end. In both numerical and experimental data, the potential core zone is smaller than $0.2a$. The rapid drop of the centerline velocity observed in the numerical solution for $(x - \Delta)/a > 8$ is attributed to the effect of the absorbing boundary scheme used in the model. In fact, although the nominal thickness of the absorbing boundary was set to 15 lattice cells, the effective absorbing region is considerably greater than its prescribed thickness value, depending on the flow velocity, as discussed in [42].

An exact analytical solution for the transverse velocity profile of a round fully developed laminar free jet in the similarity zone was proposed by Schlichting [43]. The solution was obtained by solving the Navier–Stokes equations, taking into account symmetry, and using boundary-layer assumptions. However, in Schlichting's solution the jet is assumed to exit from an infinitesimally small orifice and, consequently, can only be adequately implemented at very long distances from the outlet. Experimental investigations [20,21] have shown that the behavior of a laminar axisymmetric jet in the similarity zone can be well approximated by a Gaussian distribution of the form

$$\frac{u_x}{u_0} = \frac{u_{cl}}{u_0}\exp\left(\frac{-r^2}{2\sigma^2}\right),\tag{27}$$

where σ is the r-coordinate at which $u_x = 0.605u_{cl}$. Fig. 6 depicts results for the transverse velocity profiles obtained within the similarity zone at different downstream distances from the pipe's exit measured in terms of pipe radii. The dashed lines
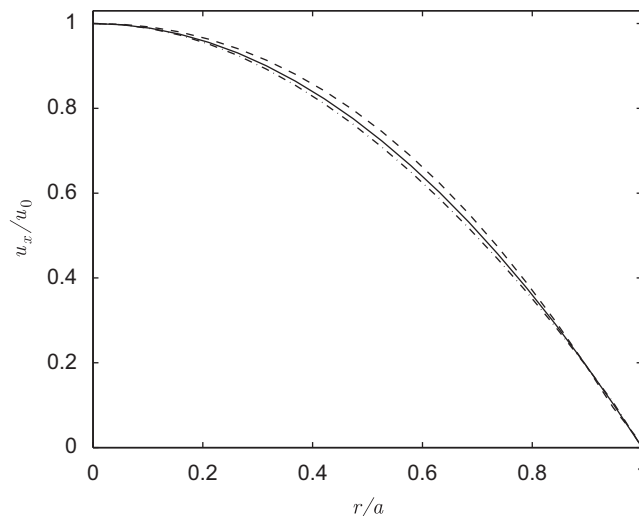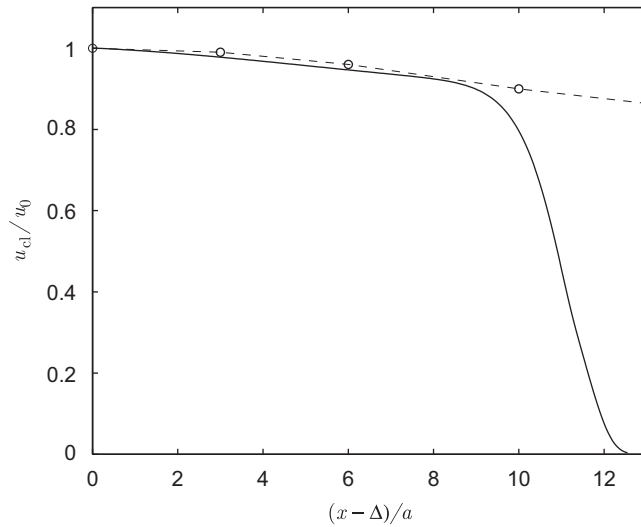

Fig. 4. Normalized axial velocity profile inside the pipe as a function of the dimensionless axial position. The numerical results at $x = 0$ (-·-) and at $x = \Delta$ (- - -) are obtained for $Re = 441$ and $M = 0.15$ and the theoretical values (—) are obtained from Eq. (26).

Fig. 5. Normalized centerline velocity decay as a function of the dimensionless distance from the open end. The numerical results (—–) are obtained for $M = 0.15$ and $Re = 441$. The experimental data (-○-○-) provided by Symons and Labus for a laminar free jet at $Re = 437$.
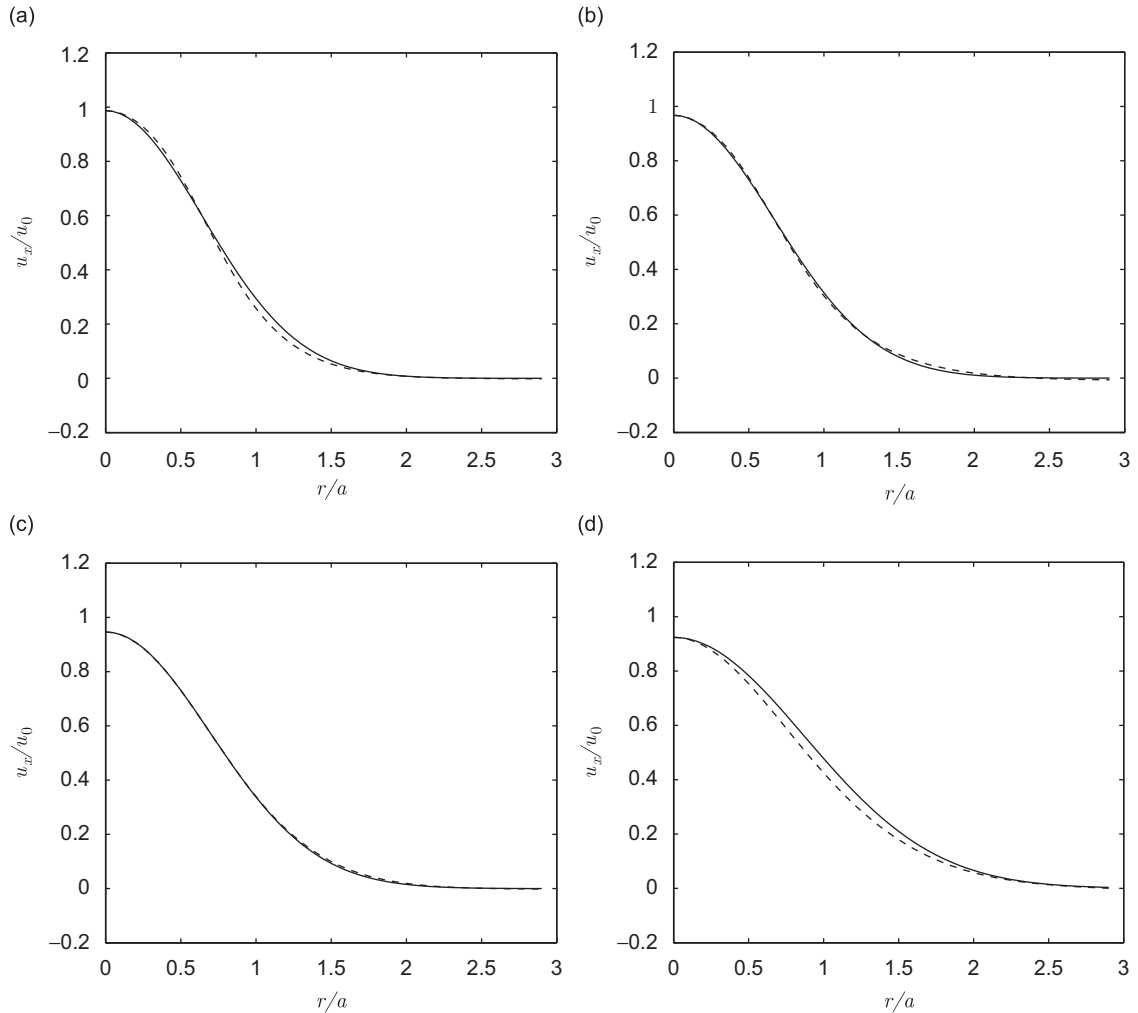
Fig. 6. Normalized velocity profiles at different downstream distances from the open end as functions of the dimensionless radial coordinate r/a. (- - -) are the numerical results, and (—) are the values given by Eq. (27). The values are obtained for four different downstream distances from the open end: (a) $2a$; (b) $4a$; (c) $6a$; and (d) $8a$.
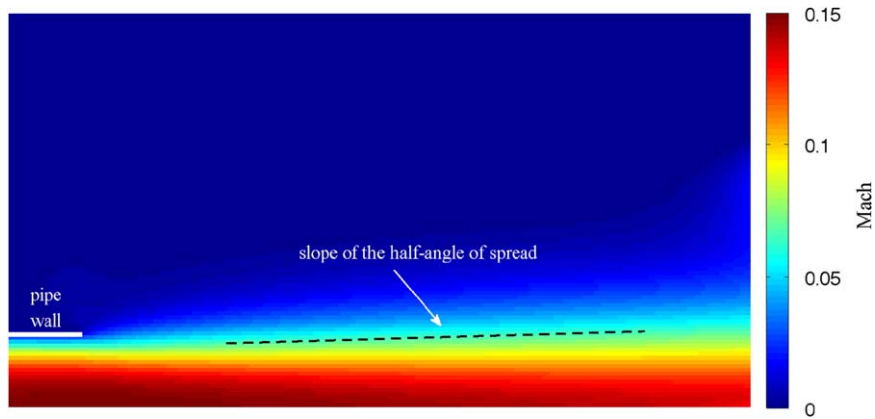
Fig. 7. Instantaneous snapshot of the velocity magnitude of the flow field in terms of Mach number. The dashed slope represents the best linear fit for the half-angle of spread.

represent the numerical values and the solid lines are obtained from Eq. (27), using values of σ, u_0 and u_{cl} obtained numerically.

The numerical results in Fig. 6 match considerably well the Gaussian distribution provided by Eq. (27), except for slight deviations encountered in Figs. 6(a) and (d). The small discrepancy found in the first case (Fig. 6(a)) is explained by the fact that the flow at this distance from the pipe's open end is still in the transition region between the core zone and the similarity zone. In the second case (Fig. 6(d)), the numerical velocity profile is slightly degraded by the effect of the absorbing boundary condition, as in the case of the centerline velocity decay (Fig. 5).

The spreading of the jet obtained in the numerical calculations for $Re = 441$ is compared with the experimental results provided by Symons and Labus [20] for the same type of jet at $Re = 437$. The comparison is conducted in terms of half-angle of spread θ, which is the angle between the pipe axis and the slope formed by a linear fit between the values of σ along the similarity zone. The half-angle of spread obtained numerically is assessed from the slope calculated between 2 and 8 radii from the pipe's open end, as depicted as a black dashed line in Fig. 7. The resulting value of $\theta = 2.3°$ agrees reasonably well with the experimental value $\theta = 2°$ observed by Symons and Labus [20,21].

The results provided in Figs. 4–7 indicate that the numerical axisymmetric scheme proposed in this paper can correctly capture the upstream and downstream behaviors of the flow at $M = 0.15$. In the case of the downstream region, this is particularly true for a very short distance from the open end, namely before eight radii. As it will be seen, however, such short downstream region is satisfactory to attain the wave reflection phenomena inside the pipe, as investigated in this paper.
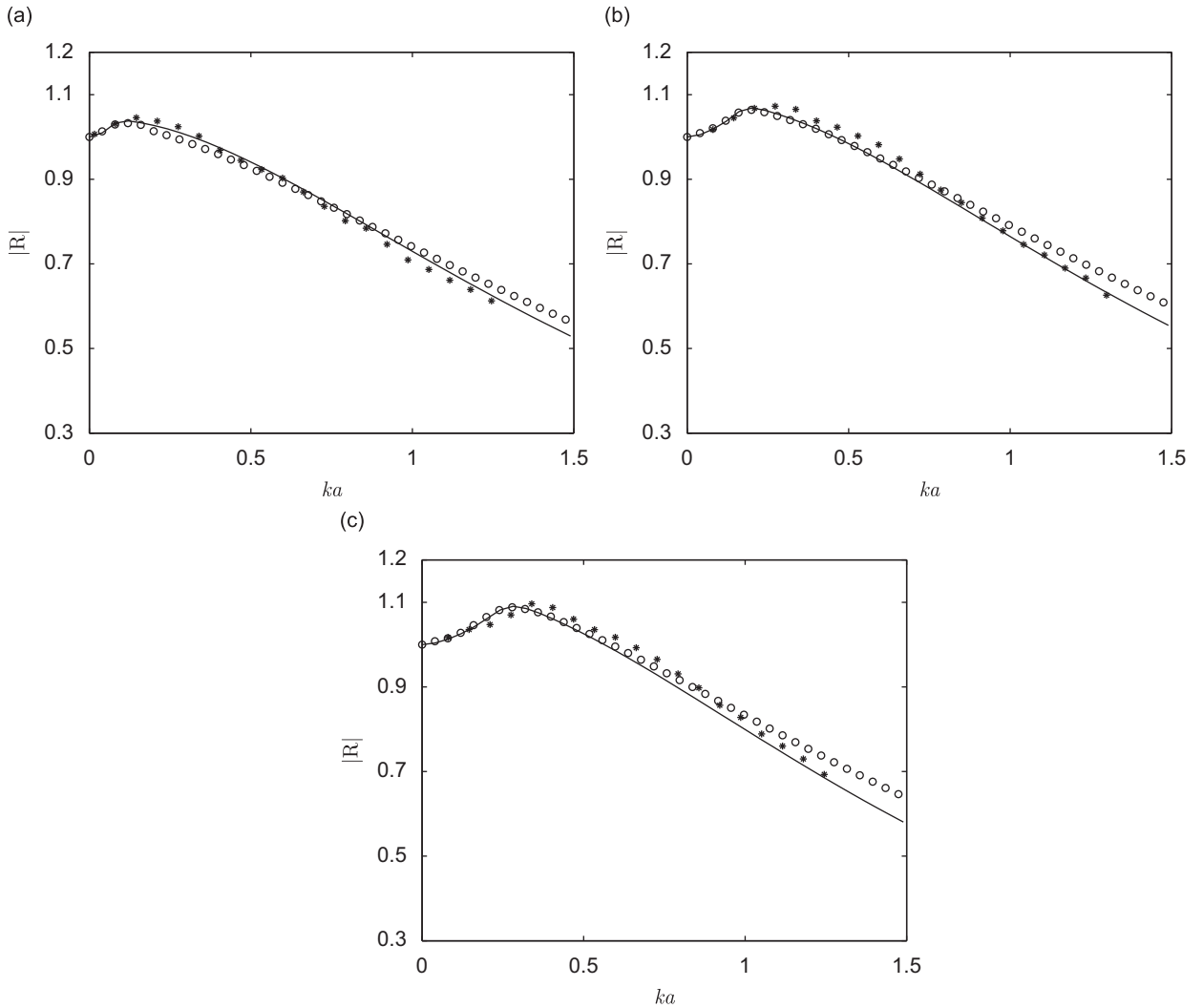
5.2. Sound reflection at the open end

The following results take into account the effect of the acoustic source applied to the closed end of the pipe, as described in Section 4.1. The graphics in Fig. 8 depict the results for the magnitude of the reflection coefficient $|R|$ at the open end, plotted as a function of the Helmholtz number ka for different Mach and Reynolds numbers. In general, the numerical results agree very well with the theoretical and experimental data provided by Munt [13] and Allam and Åbom [14].

The reflection gain represented by the regions where $|R| > 1$ is also well predicted by the model. In general, better agreement is found for low Mach and Helmholtz numbers. The highest discrepancy from the theory is ∼6 percent at $ka = 1.5$ for $M = 0.15$ (Fig. 8). As the Mach number decreases to 0.05, the highest deviation becomes <1 percent at $ka = 1.5$.

The deviation of the simulation from the theoretical and experimental results at high Mach number is attributed to the limit of compressibility of the LBGK scheme. As demonstrated by Halliday [34] and by Reis and Phillips [35], the Navier–Stokes equations in polar coordinates (Eqs. (7)–(9)) can be fully recovered from the axisymmetric lattice Boltzmann scheme used in this study for the low compressibility limit, more precisely for $M \leq 0.15$. The simulations performed for $M = 0.15$ are thus at the upper limit of this range and the accuracy is likely degraded to some extent. The discrepancy found in the high frequencies may be associated with an insufficient number of lattice cells per wavelength.

Similar to the experimental results reported in [14], better agreement with the theory is achieved when the Mach number values associated with the predictions of $|R|$ are calculated based on the maximum flow speed inside the pipe, that is $u_0 = u_x(\Delta, 0)$. As explained in [14], the better agreement found for u_0 comes from the fact that Munt's model assumes a uniform (plug) flow, meaning that the convection speed of the vortical instabilities downstream from the duct opening is

Fig. 8. Magnitude of the pressure reflection coefficient |R| at the open end as a function of the Helmholtz number $ka = 2\pi fa/c_0$ for different Mach numbers. The numerical results (○) are compared with the analytical data (—–) from Munt's model and with the experimental data (∗) from Allam and Åbom: (a) $Re = 147$, $M = 0.05$; (b) $Re = 294$, $M = 0.10$; and (c) $Re = 441$, $M = 0.15$.

given by $Mc_j/2$ when the external fluid is stagnant. In the case of both a real jet and the present simulations, however, the flow profile is non-uniform and the convection speed of the instabilities is given by $\sim u_0/2$ [44]. Thus, it is reasoned that one should choose the maximum jet velocity u_0 as the reference for the correct calculation of the vortex convection speed, instead of using the cross-section averaged value of flow velocity.

Fig. 9 presents the same results of the magnitude of the reflection coefficient |R| as a function of the Strouhal number $Sr_0 = ka/M$. In this case, the peaks of all the curves have their maximum at $Sr_0 \sim \pi/2$. This value is half of that predicted by the approximate theory proposed by Cargill [7] but obviously agrees with the theoretical and measured results of Munt [13] and Allam and Åbom [14], respectively.

An interesting way to explain the physical meaning of the peak region is obtained by manipulating the relation $Sr_0 = ka/M \sim \pi/2$, which leads to

$$T \sim 4a/\bar{u}_x, \tag{28}$$

where T is the oscillation period of the acoustic source. Considering that the propagation velocity of the vortical instabilities u_v at the vortex sheet of a jet in a stagnant fluid is given by $u_v \sim \bar{u}_x/2$ [44], the above relation becomes

$$T \sim D/u_v, \tag{29}$$

where D is the pipe diameter. Eq. (29) implies that the maximum reflection coefficient magnitude occurs when the oscillation period of the acoustic source is approximately equal to the time necessary for the vortical instabilities to propagate a distance equal to the pipe diameter D.
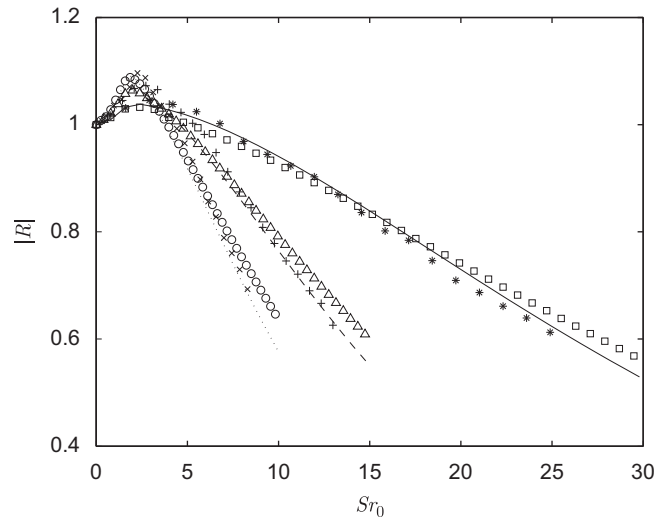
Fig. 9. Comparison between the numerical solution, experimental data of Allam and Åbom and theoretical predictions by Munt for the reflection coefficient magnitude $|R|$ as a function of the Strouhal number $Sr_0 = ka/M$ for different Mach numbers. For $Re = 147$ and $M = 0.05$, $\square\square\square$ is the numerical result; $***$ is the experimental data; and —- is the theoretical prediction. For $Re = 294$ and $M = 0.10$, $\triangle\triangle\triangle$ is the numerical; $+++$ is the experimental data; and - - - is the theoretical prediction. For $Re = 441$ and $M = 0.15$, $\circ\circ\circ$ is the numerical solution; $\times\times\times$ is the experimental data; and $\cdots$ is the theoretical prediction.
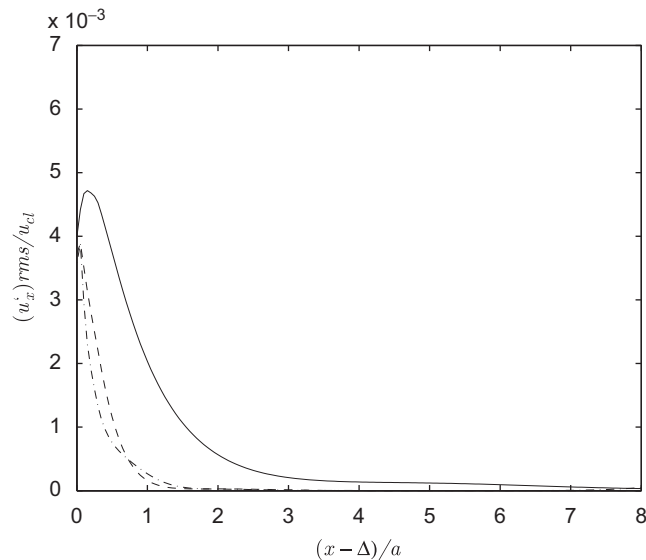
Fig. 10. Time-averaged axial turbulence intensity along the jet shear layer for different flow velocities. —-, $M = 0.15$ and $Re = 441$; - - -, $M = 0.10$ and $Re = 294$; and -·-, $M = 0.05$ and $Re = 147$.

According to the theory [13], values of the reflection coefficient greater than one are caused by the transfer of kinetic energy from the flow to the acoustic field due to the interaction of the unstable vortex sheet with the lip of the pipe. The instability of the vortex sheet is, in turn, triggered by the sound transmitted through the open end. Fig. 10 presents the time-averaged axial turbulence intensities along the pipe's lip-line for different flow velocities and an acoustic source frequency $f_s = u_v/D$, which corresponds to the maximum transfer of kinetic energy from the flow to the acoustic field at $Sr_0 = \pi/2$. As predicted by the theory, the peaks of turbulence intensity take place very close to the rim of the pipe. The maximum value of the turbulence intensity was 0.5 percent for $M = 0.15$. For both $M = 0.10$ and 0.05, the obtained turbulence intensity was 0.4 percent.

Fig. 11 provides a qualitative description of the interaction of the unstable vortex sheet with the lip of the pipe by depicting instantaneous snapshots of the flow stream lines (in blue) superimposed on the velocity field (in red) at the pipe exit for $M = 0.15$ and $f_s = u_v/D$. The snapshots were taken for different intervals within a single oscillation cycle of the
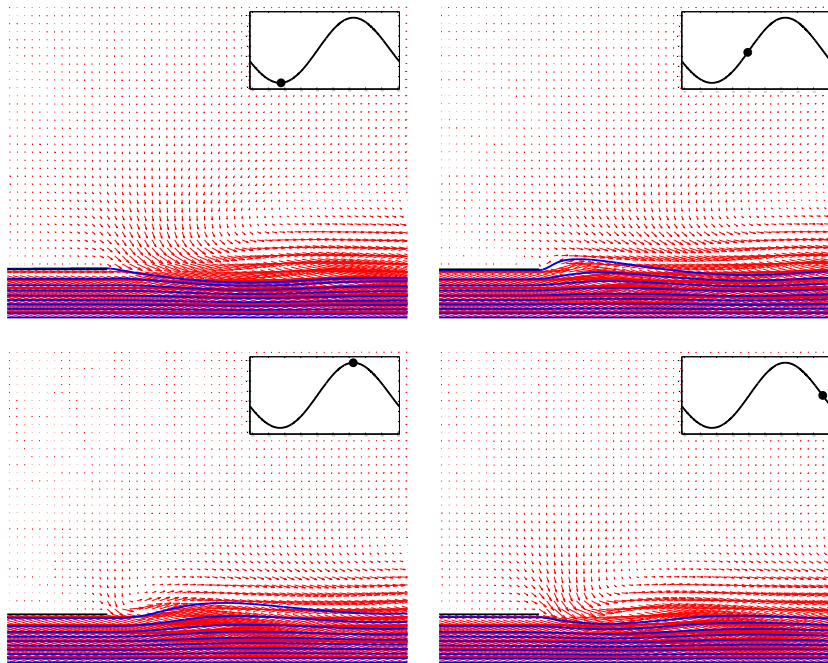
Fig. 11. Mean flow visualization for $M = 0.15$, $Re = 441$, and $u'_x/u_x = 0.1$ at the pipe open end for different time frames within a single oscillation period. The boxes on the top indicate the frame position in terms of the flow velocity cycle measured at the open end. The stream lines are depicted in blue and red arrows indicate the velocity field. (For interpretation of the references to color in this figure legend, the reader is referred to the web version of this article.)

space-averaged particle velocity u'_x, measured across the pipe's open end. The fraction of the oscillation cycle of u' associated with each snapshot is depicted at the upper right corner of each figure.

Fig. 12 provides a comparison between numerical, theoretical and experimental results for the dimensionless end correction as a function of the Helmholtz number. In this case, the most significant influence of the mean flow is to strongly reduce the values of the end correction when $ka \rightarrow 0$.

In general, the numerical results agree very well with Munt's theory, specifically at the high frequency limit ($ka > 0.5$) for which the dimensionless end correction values approximate those obtained for the same pipe carrying a zero mean flow [5]. In the low frequency region ($ka < 0.5$), where the effect of the mean flow becomes significant, the numerical results diverge slightly from the theory. Interestingly, a similar discrepancy is found for the experimental results and can be attributed to the effect of the finite wall thickness used in both the experimental and numerical evaluations as opposed to the infinitely thin wall assumed by the theory. Previous investigations reported in [37,42] suggest that the discrepancy between numerical and theoretical predictions is diminished as $(a - w_t)/a \rightarrow 1$, where w_t is the constant wall thickness of the pipe, equal to one lattice cell. Naturally, this is achieved by decreasing the lattice pitch Δx and consequently, augmenting the computational cost. As reported by Peters et al. [12] and Atig [45], the end correction seems to be much more sensitive to small geometric details than the magnitude of the reflection coefficient $|R|$. Moreover, the small discrepancies between the numerical results and those provided by the theory and experiments seem to increase with the Mach number for the entire range of ka. This is because the simulations approach the low compressibility limit ($M \rightarrow 0.15$) for which the full Navier–Stokes equations can be recovered from the lattice Boltzmann equation, as discussed previously.

Fig. 13 depicts the same curves of the dimensionless end correction plotted as a function of the Strouhal number Sr_0. At low Strouhal numbers ($Sr_0 < \pi$) the graphs for different Mach numbers tend to collapse into a single curve and $l/a \rightarrow 0.2554\sqrt{1 - M^2}$ as $ka \rightarrow 0$, which is the low limit value predicted by Rienstra [46].

6. Results for circular horns

The effects of circular horns on the parameters associated with the reflection coefficient are now presented. The following results were obtained at the junction between the pipe and the horn ($x = \Delta$) in accordance with the experiments carried out by Peters et al. [12]. The two different horn sizes considered in this paper are defined by the horn curvature radii $r_h = 2a$ and $r_h = 4a$, as depicted by dashed lines in Fig. 3.

Fig. 14 depicts the effect of the mean flow on the behavior of the reflection coefficient magnitude $|R|$ as a function of the Helmholtz number ka for the two different circular horns considered.

From a qualitative standpoint, the effect of the mean flow on $|R|$ is found to be similar to that encountered for the unflanged pipe discussed in Section 5.2. That is to say, the influence of the mean flow is only significant for low Helmholtz
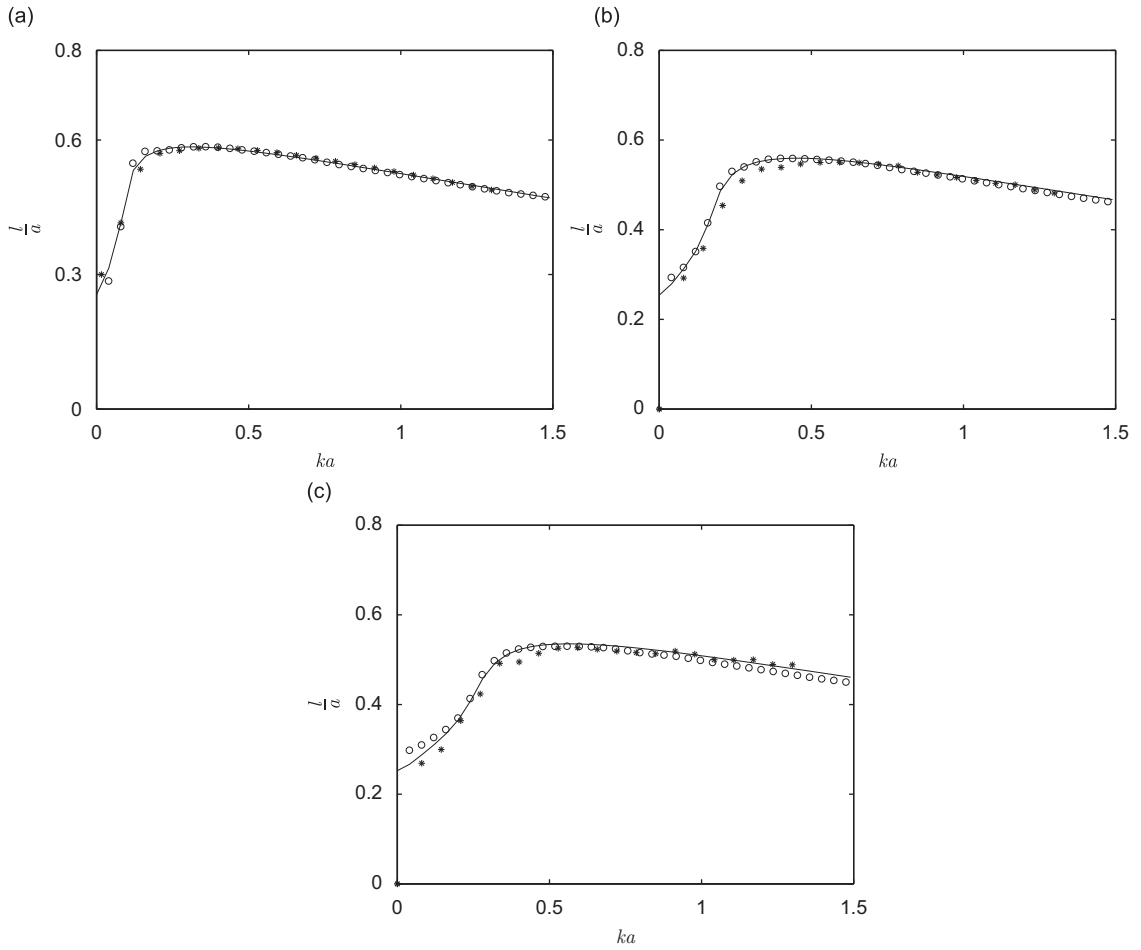
Fig. 12. Dimensionless end correction l/a as a function of the Helmholtz number $ka = 2\pi fa/c_0$ for different Mach numbers. The numerical results ($\circ$) are compared with the analytical data (—–) from Munts's model and with the experimental data ($*$) from Allam and Åbom: (a) $M = 0.05$, $Re = 147$; (b) $M = 0.10$, $Re = 294$; and (c) $M = 0.15$, $Re = 441$.
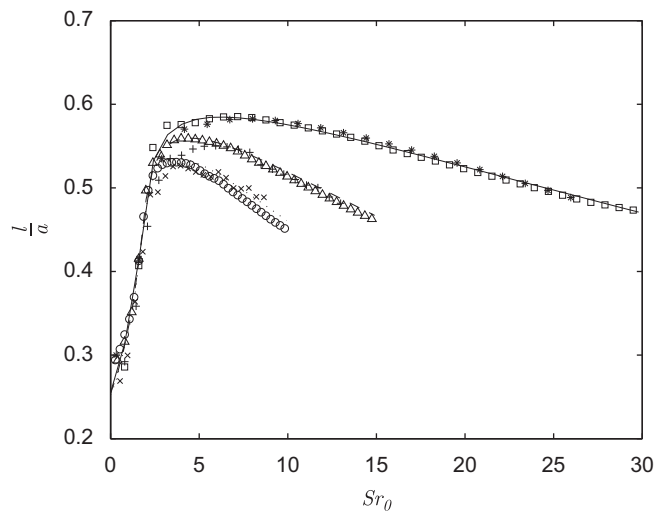

Fig. 13. Comparison between the numerical solution, experimental data [14] and theoretical predictions [13] for the dimensionless end correction l/a as a function of the Strouhal number $Sr_0 = ka/M$ for different Mach numbers. For $M = 0.05$ and $Re = 147$, $\square\square\square$ is the numerical result; $***$ is the experimental data; and —– is the theoretical prediction. For $M = 0.10$ and $Re = 294$, $\triangle\triangle\triangle$ is the numerical; $+++$ is the experimental data; and - - - is the theoretical prediction. For $M = 0.15$ and $Re = 441$, $\circ\circ\circ$ is the numerical solution; $\times\times\times$ is the experimental data; and $\cdots$ is the theoretical prediction.
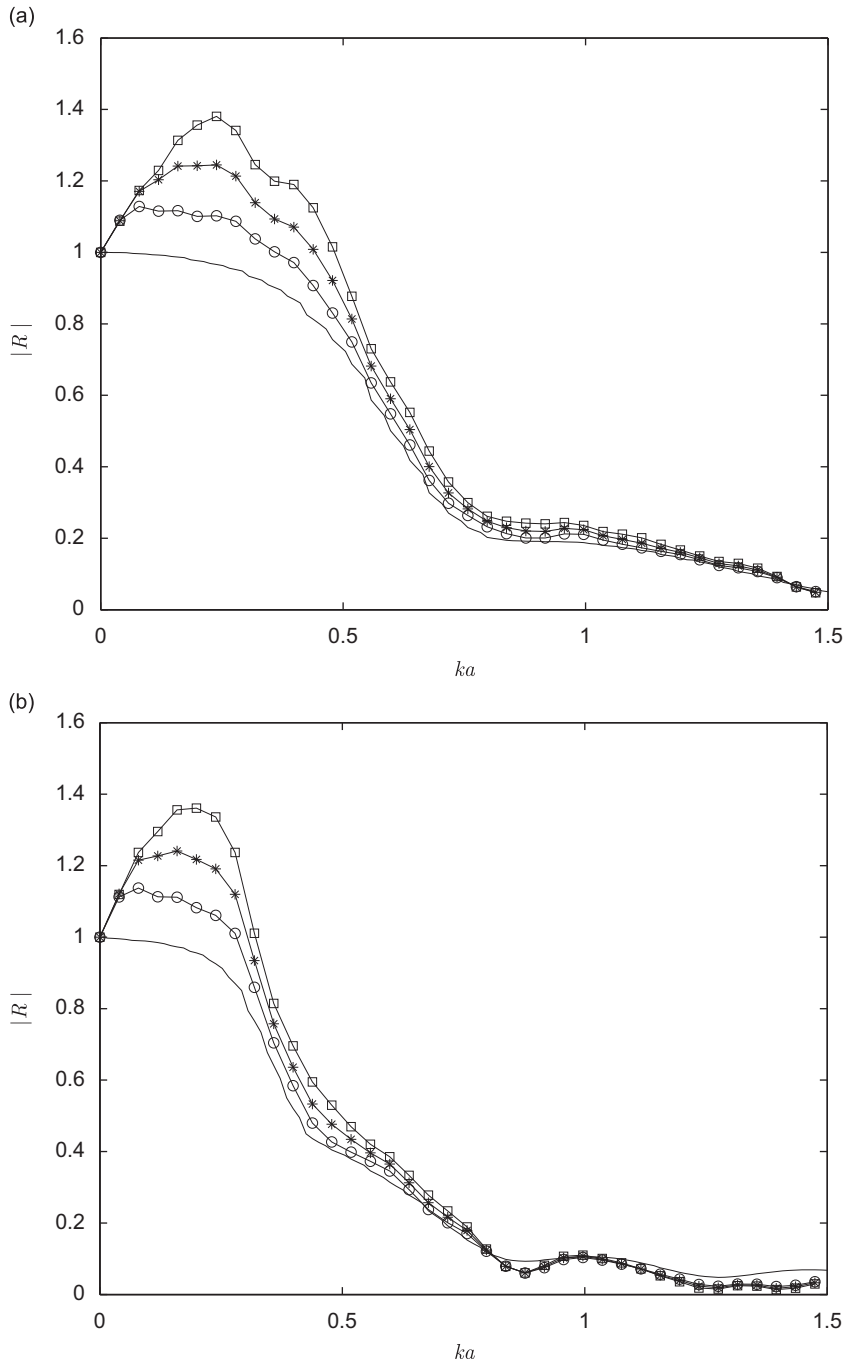
Fig. 14. Numerical results for the reflection coefficient magnitude $|R|$ at the end of the pipe as a function of the Helmholtz number $ka = 2\pi fa/c_0$ for two different horn curvature radii r_h and different Mach numbers: (a) $r_h = 2a$; and (b) $r_h = 4a$. The line $-\square-$ corresponds to $M = 0.15$ and $Re = 441$; $-*-$ corresponds to $M = 0.10$ and $Re = 294$; $-\circ-$ corresponds to $M = 0.05$ and $Re = 147$; and $—-$ corresponds to $M = 0.0$.

numbers, namely $0 < ka < 0.5$. In this region, $|R|$ assumes values greater than one and $|R| \to 1$ as $ka \to 0$. For higher values of ka, $|R|$ is close to the solution obtained in the absence of a mean flow.

From a quantitative point of view, however, the behavior of $|R|$ diverges considerably from the unflanged pipe case (see Fig. 8). For a given Mach number, the amplitude of the peak of $|R|$ becomes ~ 20 percent higher when a circular horn is attached to the pipe's open end. Interestingly, horns with different curvature radii present the same peak magnitude for the same Mach number. This characteristic becomes more evident when $|R|$ is plotted against the Strouhal number $Sr_0 = ka/M$, as depicted in Fig. 15.
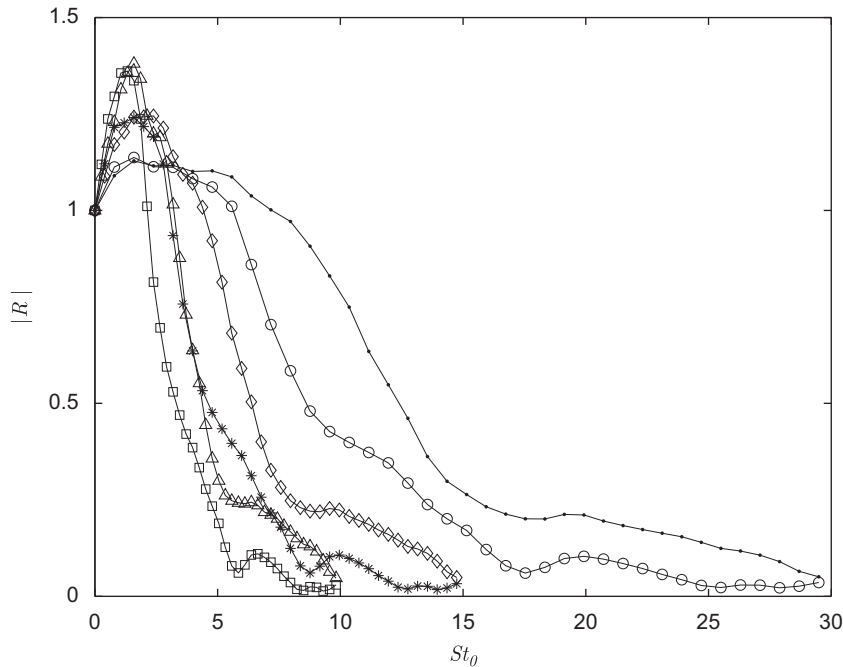
Fig. 15. Numerical results for the reflection coefficient magnitude $|R|$ at the end of the pipe as a function of the Strouhal number $Sr_0 = ka/M$ for different horn curvature radii and different Mach numbers: For $r_h = 2a$, $-\bullet-$ corresponds to $M = 0.05$; $-\diamond-$ corresponds to $M = 0.10$; and $-\triangle-$ corresponds to $M = 0.15$. For $r_h = 4a$, $-\circ-$ corresponds to $M = 0.05$; $-*-$ corresponds to $M = 0.10$; and $-\square-$ corresponds to $M = 0.15$.

In this case, the curves of $|R|$ for different horns and the same Mach number collapse into each other for $Sr_0 < 5$, which implies that, for such a region, the effect of the horn curvature is negligible and the behavior of $|R|$ is predominantly dictated by the Mach number. Furthermore, Fig. 15 shows that the maxima of $|R|$ always appear at $Sr_0 = \pi/2$, regardless of Mach number or horn curvature. This is essentially the same Strouhal number at which the maxima of $|R|$ take place in the unflanged pipe situation (see Fig. 9) but diverges from the experimental data provided by Peters et al. [12], who found the maximum magnitude of $|R|$ appears at $Sr_0 = \pi a/r$ for a circular horn with $r_h = 4a$.

The reflection phenomena at the pipe-horn junction can also be plotted in terms of the power reflection coefficient, defined as $R_E = |R|^2((1 - M)/(1 + M))^2$ as depicted in Fig. 16, which represents the ratio between outgoing and reflected acoustic power.

For the critical region $Sr_0 \sim \pi/2$ the values of $|R_E|$ become greater than unity. This behavior agrees with the experimental data of Peters et al. [12] for a horn with $r = 4a$. In their results, however, the peak of the energy reflection function was found at $Sr_0 \sim \pi/4$. In the critical Strouhal region, the reflected acoustic power is greater than its outgoing counterpart. This paradox is explained by the transfer of kinetic energy from the unsteady vortex sheet to the acoustic field inside the pipe and it is similar to the phenomenon in unflaged pipes. Nevertheless, in the case of pipes terminated by flaring horns, the mechanism of energy transfer from the flow to the acoustic field seems to be much more effective.

Peters et al. [12] explain that the maximum energy transfer happens when the traveling time of the vortical instabilities across the horn matches the acoustic oscillation period of the acoustic source. According to this rationale, the location of the peak would be dependent on the horn curvature r_h. As previously discussed, however, our results suggest that the region of maximum transfer is independent of the horn geometry. In this case, the explanation given in the previous section for the region of maximum energy transfer in the case of unflanged pipes can be generalized to pipes terminated by circular horns. That is, the maximum reflection coefficient happens when the oscillation period of the acoustic source is approximately equal to the time necessary for the vortical instabilities to propagate a distance equal to the pipe diameter D, as expressed in Eq. (29).

Fig. 17 shows the time-averaged turbulence intensities along the jet's vortex sheet for one oscillation cycle at $Sr_0 = \pi/2$. In contrast to the unflanged pipe case, the peaks of turbulence intensity caused by the instabilities of the vortex sheet take place at different distances away from the pipe's termination but before the open end of the horns. The location of the peaks is proportional to the horn's curvature radius, and slightly proportional to the velocity of the flow u_x. In general, for the same flow velocity, the horn with the curvature radius $r = 4a$ presents the peak of turbulence intensity shifted towards the open end by $0.3a$ (Fig. 17(b)), when compared to the horn with $r = 2a$ (Fig. 17(a)). The amplitude of the turbulence intensity seems to be also proportional to the horn curvature radius. The maximum results for the turbulence intensity for $M = 0.15$ correspond to 1.43 and 1.52 percent for $r = 2a$ and $r = 4a$, respectively. These turbulence intensity values are considerably higher than those found for an unflanged pipe with the same flow conditions.
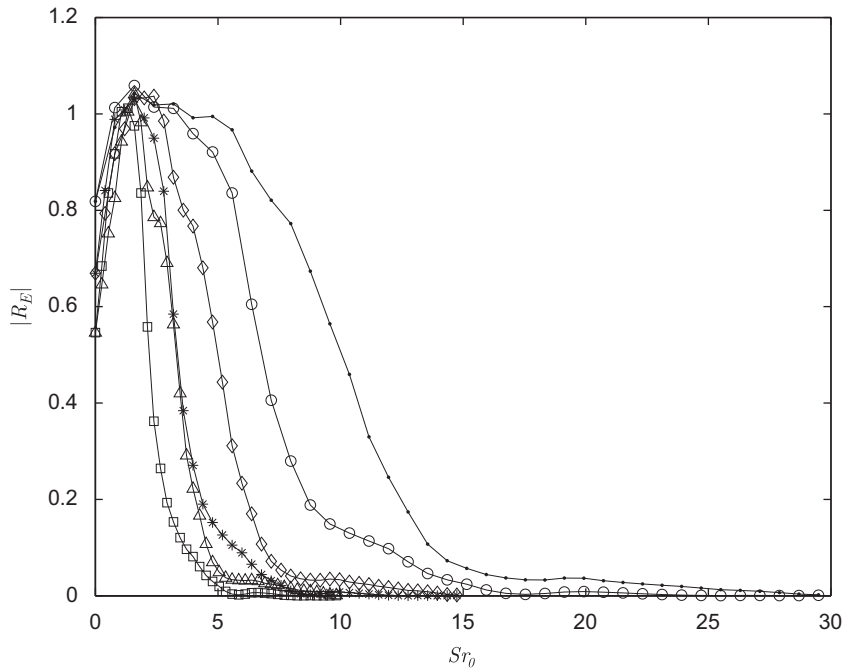
Fig. 16. Numerical results for the energy reflection coefficient $|R_E|$ at the end of the pipe as a function of the Strouhal number $Sr_0 = ka/M$ for different horn curvature radii and different Mach numbers: For $r_h = 2a$, $-\bullet-$ corresponds to $M = 0.05$; $-\diamond-$ corresponds to $M = 0.10$; and $-\triangle-$ corresponds to $M = 0.15$. For $r_h = 4a$, $-\circ-$ corresponds to $M = 0.05$; $-*-$ corresponds to $M = 0.10$; and $-\square-$ corresponds to $M = 0.15$.

(a)   (b)
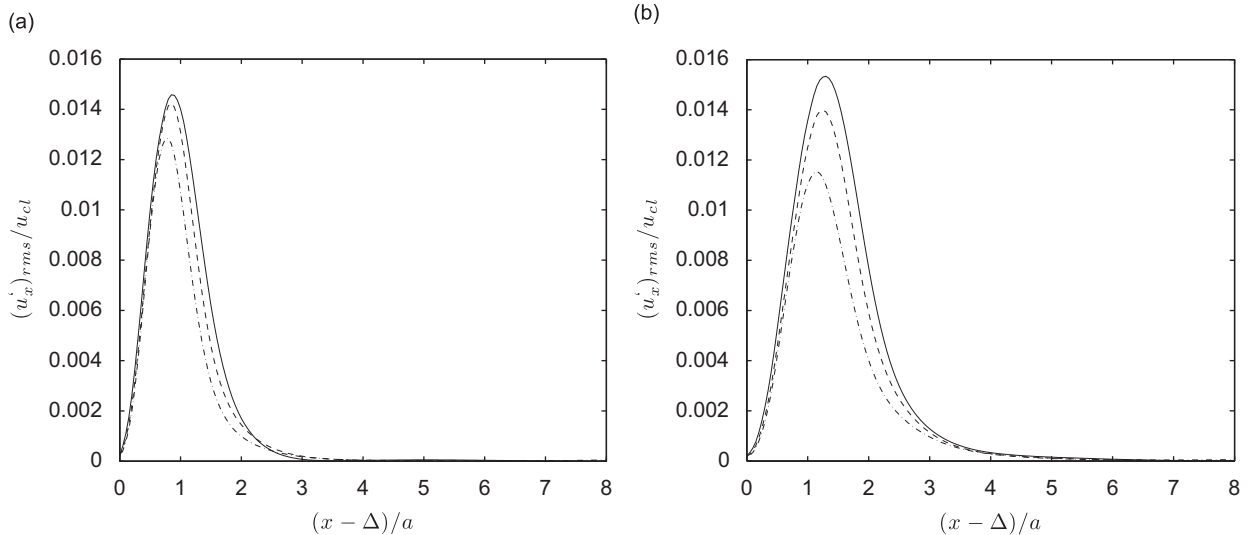
Fig. 17. Downstream time-averaged axial turbulence intensity along the jet shear layer for different flow velocities. — $M = 0.15$ and $Re = 441$; - - - $M = 0.10$ and $Re = 294$; and $-\cdot\cdot-$ $M = 0.05$ and $Re = 147$: (a) $r = 2a$; and (b) $r = 4a$.

A qualitative description of the flow field is presented in Fig. 18 by showing instantaneous snapshots of the vortex sheet instabilities triggered by the acoustic field during one oscillation cycle for the two horn curvatures analyzed in this paper. The snapshots are presented in terms of stream lines (in blue) superimposed on the velocity field (in red) for $M = 0.15$ and $Sr_0 = \pi/2$. An interesting aspect observed in both horn curvatures is the adhesion/separation of the jet on the horn wall caused by the instability of the pressure gradient. As it will be discussed in the next section, the adhesion/separation of the jet on the walls partially explains the augmentation of the turbulence intensity in the case of pipes terminated by horns (Fig. 17), as opposed to unflanged pipes (Fig. 10).

(a)   (b)
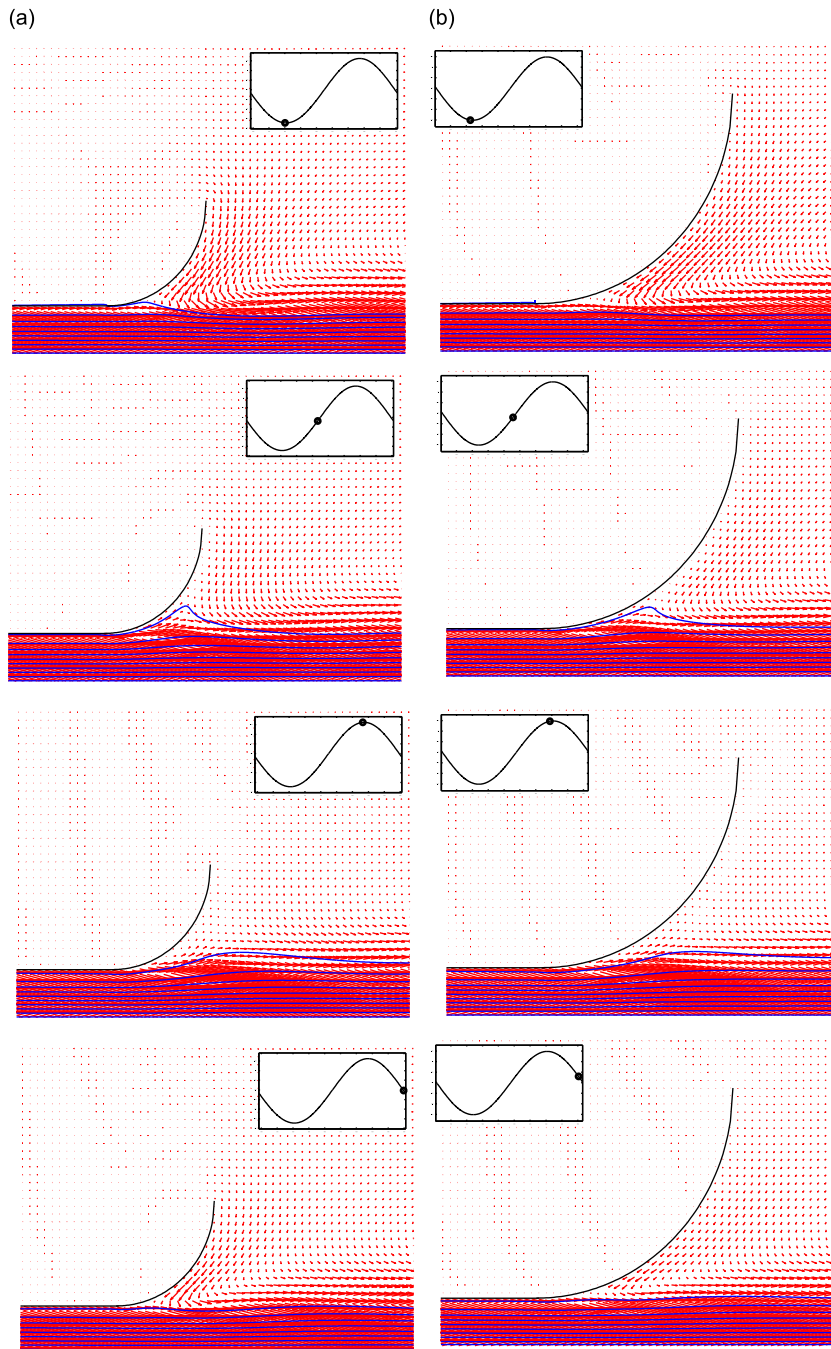
Fig. 18. Mean flow visualization at the output of the pipe-horn system at different time frames within a single oscillation period for $M = 0.15$ and $Re = 441$. The boxes on the top indicate the frame position in terms of the flow velocity cycle measured at the pipe-horn junction. The stream lines are depicted in blue and red arrows indicate the velocity field: (a) $r = 2a$; (b) $r = 4a$. (For interpretation of the references to color in this figure legend, the reader is referred to the web version of this article.)

The dimensionless end correction l/a as a function of ka is presented in Fig. 19 for different Mach numbers and for the two different horn geometries.

The general behavior agrees with that found for a pipe with an unflanged termination. That is, the effect of a mean flow appears to be only relevant in the low frequencies, namely before the end correction maxima found at $ka \sim \pi/2\kappa$ for both geometries, where $\kappa = r/a$. In this region, the end correction drops dramatically. Moreover, the magnitude of the end correction maxima is independent of the flow velocity. This behavior is the opposite of that found for the reflection coefficient magnitude, for which the flow velocity plays a preponderant role on the amplitude of the peaks. For higher

(a)

(b)
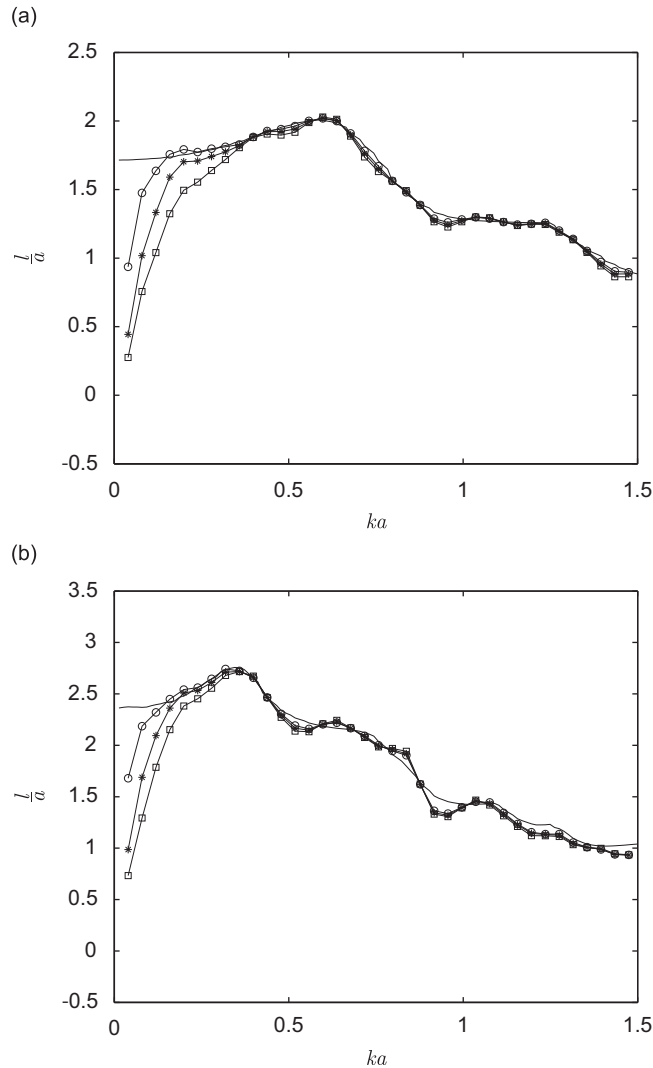
Fig. 19. Numerical results for the dimensionless end correction l/a at the end of the pipe as a function of the Helmholtz number $ka = 2\pi fa/c_0$ for two different horn curvature radii r_h and different Mach numbers: (a) $r_h = 2a$; and (b) $r_h = 4a$. The line $-\square-$ corresponds to $M = 0.15$ and $Re = 441$; $-*-$ corresponds to $M = 0.10$ and $Re = 294$; $-\circ-$ corresponds to $M = 0.05$ and $Re = 147$; and $—-$ corresponds to Re and $M = 0.0$.

frequencies, namely $ka > \frac{1}{2}\pi/\kappa$, the effect of the mean flow becomes negligible and the results approximate the solution obtained for the same terminations in the absence of a mean flow.

Fig. 20 presents the results for l/a at the pipe-horn junction plotted as functions of the Strouhal number. For $Sr_0 < \pi/2$ the graphs obtained for a given geometry and different Mach numbers collapse into a single curve. As $Sr_0 \to 0$, l/a tends to converge to very low values, namely ~ 0, for the termination with curvature $r_h = 2a$, and ~ 0.2 for the termination whose curvature is $r_h = 4a$. For the last case, Peters et al. [12] found experimentally a negative value $l/a \sim -0.25$ and a maximum value of ~ 2.3.

7. Discussion and conclusions

A numerical technique based on an axisymmetric lattice Boltzmann scheme to predict the parameters associated with the acoustic reflection at the open end of axisymmetric ducts issuing a low Mach number cold subsonic mean flow was presented in this paper. Following that, the technique was used to investigate the behavior of the pressure reflection coefficient at the open end of a cylindrical pipe terminated by circular horns of different curvature radii.

The verification of the technique was assessed by comparing the simulation results for the flow and acoustic fields of an unflanged pipe model issuing a subsonic jet into a stagnant fluid region with those provided by theory [20,13] and experiments [20,14]. Very good agreement was found with theoretical and experimental results. The agreement is particularly remarkable in the validation of the acoustic field, considering that the theory assumes an infinitely thin vortex
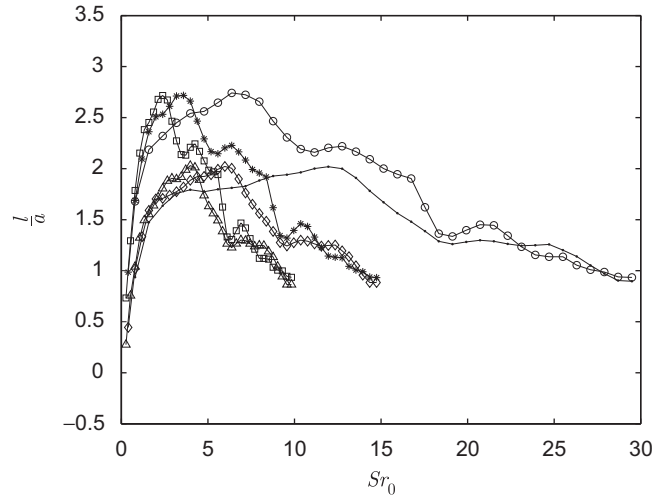
Fig. 20. Numerical results for the dimensionless end correction l/a at the end of the pipe as a function of the Strouhal number $Sr_0 = ka/M$ for different horn curvature radii and different Mach numbers: For $r_h = 2a$, $-\bullet-$ corresponds to $M = 0.05$; $-\diamond-$ corresponds to $M = 0.10$; and $-\triangle-$ corresponds to $M = 0.15$. For $r_h = 4a$, $-\circ-$ corresponds to $M = 0.05$; $-\ast-$ corresponds to $M = 0.10$; and $-\square-$ corresponds to $M = 0.15$.

sheet separating the issuing jet and the exterior stagnant fluid. However, in real situations, as well as in the numerical simulations presented here, the thickness of the vortex sheet increases as the jet travels downstream from the open end due to flow entrainment.

Analogous simulations were carried out to investigate the behavior of the pressure reflection coefficient when circular horns having different curvature radii are connected to the pipe's open end. From a qualitative point of view, the results for the horn carrying a subsonic mean flow indicate a very similar behavior to those found for an unflanged pipe. That is to say, the peak value of the magnitude of the reflection coefficient takes place at the same region given by $T \sim D/u_v$, regardless of the geometric characteristics of the open end. Moreover, in both the unflanged pipe and the pipes terminated by horns, the effect of the mean flow on $|R|$ and l/a becomes negligible at high frequencies ($ka > 0.5$). For this region, results approximate the solutions obtained for the zero mean flow situation provided in [5], for a unflanged pipe, and the numerical solutions in [47], for pipes terminated by different circular horns.

From a quantitative perspective, however, significant differences are found between an unflanged pipe and a pipe terminated by a horn in terms of l/a and $|R|$. At low Helmholtz numbers, the effect of a horn acts to provide a much more substantial reduction on the dimensionless end correction when compared to a unflanged pipe. Furthermore, the greater the curvature radius of the horn is, the greater the reduction on the end correction. This behavior is essentially the opposite of that found for the reflection coefficient magnitude $|R|$. In that case, the influence of the horn curvature is negligible at low Helmholtz and Strouhal numbers.

Another striking difference between the unflanged pipe and pipes terminated by circular horns is found near the maxima of the reflection coefficient magnitude. For the same flow conditions, pipes terminated by horns have peaks that are ~20 percent higher than those found for unflanged pipes, regardless of the horn curvature radius.

In both cases, the gain of $|R|$ is a consequence of the transfer of kinetic energy from the flow to the acoustic field. This happens because the instability caused by the acoustic field $\mathbf{u}'$ induces the roll up of the vortex sheet into regions of concentrated vorticity at the open end, which in turn produce acoustic energy. A formal description for the transfer of vortical kinetic energy into the acoustic field for low Mach number and isentropic flows is provided by Howe's energy corollary [48,49], expressed as

$$P' = -\rho_0 \int \overline{\mathbf{u}' \cdot (\boldsymbol{\omega} \times \mathbf{u})}\, \mathrm{d}V, \tag{30}$$

where P' is the instantaneous acoustic power and $\boldsymbol{\omega}$ is the *curl* of $\mathbf{u}$. The term $(\boldsymbol{\omega} \times \mathbf{u})$ inside the integral in the right-hand side of Eq. (30) represents the "vortex strength" and is carried over the volume V of $\boldsymbol{\omega}$. The overline indicates the time-average over one oscillation cycle.

The placement of a horn at the open end of the pipe acts to augment the vortex strength term $(\boldsymbol{\omega} \times \mathbf{u})$ and thus explain the higher gain on the reflection coefficient magnitude when compared to the unflanged pipe case. Two main reasons are responsible for the augmentation of the vortex strength in the case of horns: First, the instability of the pressure gradient triggered by the acoustic field forces a cyclic adhesion/separation of the jet at the horn walls, thereby generating additional vortical strength. The second reason may be associated with the entrainment of the surrounding fluid into the jet due to the viscous drag at the vortex sheet. For an unflanged pipe, the surrounding flow can be more easily drawn into the jet in comparison to the pipe terminated by a horn. As a result, more mass is entrained near the open end, which forces the kinetic energy in the jet to decrease. Consequently, the vortex strength is also decreased.

Acknowledgments

References

[1] G.F. Carrier, Sound transmission from a tube with flow, *Quarterly of Applied Mathematics* 13 (1956) 457–461.
[2] R. Many, Refraction of acoustic duct waveguide modes by exhaust jets, *Quarterly of Applied Mathematics* 30 (1973) 501–520.
[3] S.D. Savkar, Radiation of cylindrical duct acoustic modes with flow mismatch, *Journal of Sound and Vibration* 42 (1975) 363–386.
[4] R.M. Munt, The interaction of sound with a subsonic jet issuing from a semi-infinite cylindrical pipe, *Journal of Fluid Mechanics* 83 (1977) 609–640.
[5] H. Levine, J. Schwinger, On the radiation of sound from an unflanged circular pipe, *Physical Review* 73 (4) (1948) 383–406.
[6] A.M. Cargill, Low-frequency sound radiation and generation due to the interaction of unsteady flow with a jet pipe, *Journal of Fluid Mechanics* 121 (1982) 59–105.
[7] A.M. Cargill, Low frequency radiation from a jet pipe: a second order theory, *Journal of Sound and Vibration* 83 (3) (1982) 339–354.
[8] S.W. Rienstra, A small Strouhal number analysis for acoustic wave-jet flow-pipe interaction, *Journal of Sound and Vibration* 86 (4) (1983) 539–556.
[9] F. Mechel, W. Schiltz, J. Dietz, Acoustic impedance of a tailpipe, *Acustica* 15 (1965) 199–206 (in German).
[10] D. Ronneberger, Experimental study of the acoustic reflection coefficient at cross-section discontinuities of pipes carrying a mean flow, *Acustica* 19 (1967) 222–235 (in German).
[11] P.O.A.L. Davies, Plane wave reflection at flow intakes, *Journal of Sound and Vibration* 115 (1987) 560–564.
[12] M.C.A.M. Peters, A. Hirschberg, A.J. Reijnen, A.P.J. Wijnands, Damping and reflection coefficient measurements for an open pipe at low Mach and low Helmholtz numbers, *Journal of Fluid Mechanics* 256 (1993) 499–534.
[13] R.M. Munt, Acoustic transmission properties of a jet pipe with subsonic jet flow: I. The cold jet reflection coefficient, *Journal of Sound and Vibration* 142 (3) (1990) 413–436.
[14] S. Allam, M. Åbom, Investigation of damping and radiation using full plane wave decomposition in ducts, *Journal of Sound and Vibration* 292 (2006) 519–534.
[15] P.N. Shankar, Acoustic refraction and attenuation in cylindrical and annular ducts, *Journal of Sound and Vibration* 22 (2) (1972) 233–246.
[16] G. Gabard, J. Astley, Theoretical model for sound radiation from annular jet pipes: far- and near-field solutions, *Journal of Fluid Mechanics* 549 (2006) 315–341.
[17] X.X. Chen, X. Zhang, C.L. Morfey, P.A. Nelson, A numerical method for computation of sound radiation from an unflanged duct, *Journal of Sound and Vibration* 270 (2004) 573–586.
[18] Y. Özyörük, L. Long, Computation of sound radiating from engine inlet, *American Institute of Aeronautics and Astronautics Journal* 34 (5) (1996) 894–901.
[19] C.L. Rumsey, R.T. Biedron, F. Farassat, Ducted-fan engine acoustic predictions using a Navier–Stokes code, *Journal of Sound and Vibration* 213 (4) (1998) 643–664.
[20] E.P. Symons, T.L. Labus, Experimental investigation of an axisymmetric fully developed laminar free jet, Technical Report NASA TN D-6304, National Aeronautics and Space Administration, Cleveland, 1971.
[21] M.J. Albertson, Y.B. Dai, R.A. Jensen, H. Houser, Diffusion of submerged jets, *American Society of Civil Engineers Proceedings* 74 (10) (1948) 1571–1596.
[22] T.G. Malmström, A.T. Kirkpatrick, B. Christensen, D.K. Knappmiller, Centerline velocity decay measurements in low-velocity axisymmetric jets, *Journal of Fluid Mechanics* 246 (1997) 363–377.
[23] J. Bierkens, Calculations of the reflection coefficient of a jet pipe with subsonic jet flow, Technical Report, Marcus Wallenberg Laboratory for Sound and Vibration Research of the Royal Institute of Technology, Sweden, 2002.
[24] P. in't Panhuis, Calculations of the acoustic end correction of a semi-infinite circular pipe issuing a subsonic cold or hot jet with co-flow, Technical Report, Marcus Wallenberg Laboratory for Sound and Vibration Research of the Royal Institute of Technology, Sweden, 2003.
[25] S. Succi, *The Lattice Boltzmann Equation for Fluid Dynamics and Beyond*, Oxford University Press, Oxford, 2001.
[26] D.A. Wolf-Gladrow, Lattice Gas Cellular Automata and Lattice Boltzmann Models: An Introduction, *Lecture Notes in Mathematics*, Springer, Berlin, Heidelberg, 2004.
[27] P. Lallemand, L.S. Luo, Theory of the lattice Boltzmann method: dispersion, dissipation, isotropy, Galilean invariance and stability, *Physical Review E* 61 (2000) 6546–6562.
[28] Y. Qian, D. d'Humivres, P. Lallemand, Lattice BGK models for the Navier–Stokes equation, *Europhysics Letters* 17 (6) (1992) 479–484.
[29] Y. Qian, S. Succi, S.A. Orszag, Recent advances in lattice Boltzmann computing, *Annual Review of Computational Physics* 3 (1995) 195–242.
[30] P.L. Bhatnagar, E.P. Gross, M. Krook, A model for collision processes in gases. I. Small amplitude processes in charged and neutral one-component systems, *Physical Review* 94 (1954) 511–525.
[31] X.M. Li, R.C.K. Leung, R.M.C. So, One-step aeroacoustics simulation using lattice Boltzmann method, *AIAA Journal* 44 (1) (2006) 78–89.
[32] D. d'Humieres, I. Ginzburg, M. Krafczyk, P. Lallemand, L.S. Luo, Multiple-relaxation-time lattice Boltzmann models in three dimensions, *Philosophical Transactions of the Royal Society of London A* 360 (2002) 437–451.
[33] M. Tsutshara, H.K. Kang, A discrete effect of the thermal lattice BGK model, *Journal of Statistical Physics* 107 (1–2) (2002) 479–498.
[34] I. Halliday, L.A. Hammond, C.M. Care, K. Good, A. Stevens, Lattice Boltzmann equation hydrodynamics, *Physical Review E* 64 (2001) 011208.
[35] T. Reis, N. Phillips, Modified lattice Boltzmann model for axisymmetric flows, *Physical Review E* 75 (2007) 056703.
[36] A. Wilde, Calculation of sound generation and radiation from instationary flows, *Computers and Fluids* 35 (2006) 986–993.
[37] A.R. da Silva, G.P. Scavone, Lattice Boltzmann simulations of the acoustical radiation from waveguides, *Journal of Physics A: Mathematical and Theoretical* 40 (2007) 397–408.
[38] Y. Ando, On the sound radiation from semi-infinite circular pipe of certain wall thickness, *Acustica* 22 (1969) 219–225.
[39] M. Bouzidi, M. Firdaouss, P. Lallemand, Momentum transfer of a Boltzmann-lattice fluid with boundaries, *Physics of Fluids* 13 (11) (2001) 3452–3459.
[40] E.W.S. Kam, R.M.C. So, R.C.K. Leung, Non-reflecting boundary for one-step LBM simulation of aeroacoustics, *Proceedings of the 27th AIAA Aeroacoustics Conference*, Cambrige, MA, May 2006, pp. 1–9.
[41] F.Q. Hu, A stable, perfectly matched layer for linearized Euler equations in unsplit physical variables, *Journal of Computational Physics* 173 (2) (2001) 455–480.
[42] A.R. da Silva, Numerical Studies of Aeroacoustic Aspects of Wind Instruments, PhD Thesis, McGill University, 2008.
[43] H. Schlichting, *Boundary Layer Theory*, McGraw-Hill, New York, 1955.
[44] P. Freymuth, On transition in a separated laminar boundary layer, *Journal of Fluid Mechanics* 25 (1965) 683–704.

[45] M. Atig, Acoustic Nonlinearity at the Open End of a Pipe: Measurements, Modeling, and Applications in Wind Instruments, PhD Thesis, University of Maine, 2004 (in French).
[46] S.W. Rienstra, Acoustic radiation from a semi-infinite duct in a uniform subsonic flow, *Journal of Sound and Vibration* 92 (2) (1984) 267–288.
[47] A. Selamet, Z.L. Ji, R.A. Kach, Wave reflections from duct terminations, *Journal of the Acoustical Society of America* 109 (4) (2001) 1304–1311.
[48] M.S. Howe, On the absorption of sound by turbulence and other hydrodynamic flows, *Journal of Applied Mathematics* 32 (1–3) (1984) 187–209.
[49] M.S. Howe, *Acoustics of Fluid–Structure Interactions, Cambridge Monographs on Mechanics*, Cambridge University Press, Cambridge, New York, 1998.